Near-field iron and carbon chemistry of non-buoyant hydrothermal plume particles, Southern East Pacific Rise 15ºS

Colleen L. Hoffman[1], Sarah L. Nicholas[2, 3], Daniel C. Ohnemus[4], Jessica N. Fitzsimmons[5, 6], Robert M. Sherrell[6], Christopher R. German[7], Maija I. Heller[8], Jong-mi Lee[8], Phoebe J. Lam[8], Brandy M. Toner[1, 2]*

1- Department of Earth Sciences, University of Minnesota, Minneapolis, MN 55455, USA
2- Department of Soil, Water, and Climate, University of Minnesota, St. Paul, MN 55108, USA
3- Department of Geosciences, State University of New York at Stony Brook, Earth and Space Science Building, Stony Brook, NY 11794, USA
4- Bigelow Laboratory for Ocean Sciences, East Boothbay, ME, 04544, USA
5- Department of Oceanography, Texas A&M University, College Station, TX, 77843, USA
6- Department of Marine and Coastal Sciences and Department of Earth and Planetary Sciences, Rutgers University, Piscataway, NJ, USA
7- Department of Geology and Geophysics, Woods Hole Oceanographic Institution, Woods Hole, MA 02543, USA
8- Department of Ocean Sciences, UC Santa Cruz, Santa Cruz, CA 95064, USA

Highlights

- Particles exporting hydrothermal Fe to ocean interior investigated 0-100km off-axis
- Particles are composites of inorganic (mineral) and organic (biological) materials
- Sources of POC to plume include near-vent entrainment, sorption, in situ production
- Particle formation processes revealed here may be common to all hydrothermal plumes

Keywords

Scanning transmission X-ray microscopy (STXM), X-ray absorption near edge structure (XANES) spectroscopy, X-ray microprobe, GEOTRACES GP16, Eastern Pacific Zonal Transect

*corresponding author- toner@umn.edu

Abstract

Iron (Fe)-poor surface waters limit phytoplankton growth and their ability to remove carbon (C) from the atmosphere and surface ocean. Over the past few decades, research has focused on constraining the global Fe cycle and its impacts on the global C cycle. Hydrothermal vents have become a highly debated potential source of Fe to the surface ocean. Two main mechanisms for transport of Fe over long distances have been proposed: Fe-bearing nanoparticles and organic C complexation with Fe in the dissolved (dFe) and particulate (pFe) pools. However, the ubiquity and importance of these processes is unknown at present, and very few vents have been investigated for Fe-Corg interactions or the transport of such materials away from the vent. Here we describe the near-field contributions (first ~100 km from ridge) of pFe and Corg to the Southern East Pacific Rise (SEPR) plume, one of the largest known hydrothermal plume features in the global ocean. Plume particles (> 0.2 μm) were collected as part of the U.S. GEOTRACES Eastern Pacific Zonal Transect cruise (GP16) by *in-situ* filtration. Sediment cores were also collected to investigate the properties of settling particles. In this study, X-ray absorption near edge structure (XANES) spectroscopy was used in two complementary X-ray synchrotron approaches, scanning transmission X-ray microscopy (STXM) and X-ray microprobe, to investigate the Fe and C speciation of particles within the near-field non-buoyant SEPR plume. When used in concert, STXM and X-ray microprobe provide fine-scale and representative information on particle morphology, elemental co-location, and chemical speciation. Bulk chemistry depth profiles for particulate Corg (POC), particulate manganese (pMn), and pFe indicated that the source of these materials to the non-buoyant plume is hydrothermal in origin. The plume particles at stations within the first ~100 km down-stream of the ridge were composites of mineral (oxidized Fe) and biological materials (organic C, Corg). Iron chemistry in the plume and in the core-top suspended sediment fluff layer were both dominated by Fe(III) phases, such as Fe(III) oxyhydroxides and Fe(III) phyllosilicates. Particulate sulfur (pS) was a rare component of our plume and sediment samples. When pS was detected, it was in the form of an Fe sulfide mineral phase, composing ≤ 0.4% of the Fe on a per atom basis. The resuspended sediment fluff layer contained a mixture of inorganic (coccolith fragments) and Corg bearing (lipid-rich biofilm-like) materials. The particle morphology and co-location of C and Fe in the sediment was different from that in plume particles. This indicates that if the Fe-Corg composite particles settle rapidly to the sediments, then they experience strong alteration during settling

and/or within the sediments. Overall, our observations indicate that the particles within the first ~ 100 km of the laterally advected plume are S-depleted, Fe(III)-Corg composites indicative of a chemically oxidizing plume with strong biological modification. These findings confirm that the Fe-Corg relationships observed for non-buoyant plume particles within ~ 100 m of the vent site are representative of particles within this region of the non-buoyant plume (~100 km). These findings also point to dynamic alteration of Fe-Corg bearing particles during transport and settling. The specific biogeochemical processes at play, and the implications for nutrient cycling in the ocean are currently unknown and represent an area of future investigation.

1. Introduction

Chemically altered fluids are created by the circulation of seawater through the ocean crust at seafloor spreading centers (German and Seyfried, 2014). These vent fluids have physical and chemical characteristics different from those of the original seawater. When circulating fluids re-enter the deep ocean through hydrothermal vents they create hydrologic features called plumes that possess gradients in temperature and chemical composition. From a global perspective, the characteristics of vent fluids are variable among the 285 verified vent sites (InterRidge Vents Database 4.3); however, a few general themes emerge. Relative to deep ocean water, vent fluids have high temperature, low oxidation-reduction (redox) potential, and high dissolved metal and/or sulfur (S) concentrations. In vent fluids, redox active elements are present in chemically reduced and water soluble forms (e.g. iron ($Fe^{2+}_{(aq)}$), manganese ($Mn^{2+}_{(aq)}$), copper ($Cu^{+}_{(aq)}$), and hydrogen sulfide ($H_2S_{(aq)}$, $HS^{-}_{(aq)}$). In close proximity to vents, the supply of reduced chemical species to an otherwise oxic deep ocean allows chemosynthetic microorganisms to serve as the foundation of vent primary productivity (e.g. Dick et al., 2013; Dick and Tebo, 2010; Fisher et al., 2007; Li et al., 2014; Luther et al., 2001; Van Dover, 2000).

Transport of plume particles from sites of venting to the greater ocean requires materials to stay suspended in seawater on a time-scale that is comparable to basin-scale advection. In near-vent settings, several mechanisms for transport of hydrothermal Fe to the open ocean have been proposed: (1) nanoparticulate or colloidal solids having slow settling rates due to small size (Hsu-Kim et al., 2008; Kadar et al., 2012; Sands et al., 2012; Yücel et al., 2011); (2) uptake and

dispersal by water-column microorganisms (Dick and Tebo, 2010; Li et al., 2014); (3) complexes with dissolved organic C (DOC) or ligands (Bennett et al., 2008; Hawkes et al., 2013; Sander et al., 2007; Sander and Koschinsky, 2011); and (4) adsorption to and aggregation with particulate organic C (POC) (Breier et al., 2012; Toner et al., 2009a). It is well understood that materials sourced from vents can travel 100s to 1000s of km off-axis (Boström et al., 1969; Feely et al., 1990; Fitzsimmons et al., 2017, 2014; Lyle, 1986; Nishioka et al., 2013; Resing et al., 2015; Saito et al., 2013; Wu et al., 2011). Recently, long distance transport of plume particles—solids captured by 0.2 μm filtration—has been demonstrated for composites of Fe and organic C (Corg) (Fitzsimmons et al., 2017). The idea that the mobility and reactivity of Fe in the ocean is dependent on organic C has deep roots in the marine chemistry literature (e.g. Lewis et al., 1995; Rue and Bruland, 1995). As a community, we are now discovering that the strong biogeochemical tether between aqueous phase Fe and Corg also extends to solid phase Fe and Corg in the deep ocean (German et al., 2015; Toner et al., 2016). However, the specific interactions between Fe and Corg in plume particles have been investigated for very few vent sites globally (e.g. East Pacific Rise 9-10ºN; Breier et al., 2012; Toner et al., 2009). The implications of those interactions for the bioavailability of Fe to marine organisms are completely unknown at present.

At locations of high temperature venting, there are three major zones of particle formation that generally correlate with the residence time of materials within plumes: (1) the fresh buoyant plume has a residence time of seconds and a spatial scale of less than approximately one vertical meter; (2) the aged buoyant plume has a resident time of minutes to hours and a spatial scale up to 100s of vertical meters; and (3) the non-buoyant plume has a residence time of days to years and a spatial scale of 100s of meters to 1000s of horizontal kilometers (German and Seyfried, 2014). Within each of these zones, different physical, chemical, and biological processes dominate (Dick et al., 2013; Feely et al., 1987; Lilley et al., 1995; Reed et al., 2015). In the first zone, particle formation is caused primarily by the abrupt change in temperature experienced by the vent fluids upon contact with cold (ca. 2-3°C) deep ocean water. The solubility of minerals such as chalcopyrite ($CuFeS_2$), pyrite (FeS_2), and sphalerite (ZnS_2) are temperature dependent and mineral precipitation can be rapid in the first meter of the buoyant plume (Tivey, 2007; Tivey and McDuff, 1990). Biological activity is not thought to be an important factor in zone

one due to the short residence time and in some cases high temperatures of the vent fluids. It is important to note that this general framework does not preclude subseafloor particle formation. In the second zone, physical processes are dominated by the entrainment of deep ocean water, turbulent mixing of vent fluids and seawater, and rapid dilution of vent fluids (Jiang and Breier, 2014). Particle formation in zone two is caused by aggregation of near-vent (organic and inorganic) debris with minerals from zone one, chemical alteration of entrained debris (e.g. via reactions with hydrogen sulfide), and continued mineral precipitation based on the solubility and oxidation kinetics of metals such as Fe(III) (e.g. Adams et al., 2011; Bennett et al., 2011a, 2011b; Dymond and Roth, 1988; Field and Sherrell, 2000; Holden et al., 2012; Tivey and McDuff, 1990). The degree to which active, *in-situ* biological processes influence particle formation in zone two is not well understood; however, there is evidence that microbial cells do respond to plume conditions within this zone at some locations (Bennett et al., 2013; Sheik et al., 2015). The third zone is characterized by dilute particle concentrations, gradual chemical gradients of demonstrable hydrothermal origin, long distance transport of hydrothermally derived solutes and particles, and residence times relevant for *in-situ* biological activity (Cowen and Bruland, 1985; Dick et al., 2009; Fitzsimmons et al., 2017; Reed et al., 2015; Resing et al., 2015).

In this contribution, we describe the chemistry of hydrothermally derived particles (> 0.2 µm) within the first ~ 100 km of a non-buoyant plume sourced from the Southern East Pacific Rise (SEPR) at 15°S and points further south (Shimmield and Price, 1988). Particles were collected during the GEOTRACES Eastern Pacific Zonal Transect (EPZT, GP16) using *in-situ* filtration above the plume, within the plume, and below the plume at two sites: on-axis (Station 18) and 83 km off-axis (Station 20). A seafloor sediment sample was also collected at Station 20. Particulate Fe and C speciation were measured using two complementary X-ray synchrotron approaches: (1) scanning transmission X-ray microscopy (STXM) for imaging and C 1s and Fe 2p X-ray absorption near edge structure (XANES) spectroscopy, and (2) X-ray microprobe for X-ray fluorescence (XRF) mapping for S, Fe, and other elements, and Fe 1s XANES. The particle-specific Fe and C chemistry is complemented by depth profiles of POC, pFe, and pMn concentrations, as well as bulk C 1s, Mn 1s, and Fe 1s bulk XANES spectra for the Station 20 sediment fluff layer.

Previous investigations of plume characteristics along-axis at the SEPR observed plumes of varying Fe:S, Fe oxyhydroxide-rich plumes north of 17°20'S, and plumes with maximum Fe concentrations observed at 15°S (Feely et al., 1996). At this time, the distribution and characteristics of vents and endmember fluids along the 13°S - 17°S SEPR are unknown as previous studies have focused mainly on characterizing vent fluids between 17°S - 19°S (Charlou et al., 1996; Feely et al., 1996). There is evidence that the plume detected on-axis at 15°S (Station 18) is not the sole contributor of material to Stations 20 and all points west (Fitzsimmons et al., 2017; Resing et al., 2015; Shimmield and Price, 1988). The plume detected at Station 20 may well be an integration of hydrothermal fluxes from points as far south as 20°S. Specifically, the hydrothermal materials contributing to the plume at Station 20 may hail from a deep gyre flowing north from approximately 30°S, steered by the EPR topography, which then turns west close to 15°S (Shimmield and Price, 1988). Therefore, the observations provided here describe the particle inputs into the SEPR 4000+ km plume at the 15°S ridge axis (Station 18) as well as the integrated hydrothermal signal at Station 20.

2. Methods

2.1 Sample Collection

2.1.1 In-situ Filtration and Sample Preservation

As part of the US GEOTRACES-Eastern Pacific Zonal Transect cruise (GP16), marine particles were collected by *in-situ* filtration along a ~8000 km transect that includes greater than 4000 km of hydrothermally influenced waters. Samples from Station 18 (the ridge axis) and Station 20 (83 km west of the ridge axis) were filtered using a custom manifold attached to the deployed dual-flow McLane pumps. The overall *in-situ* pump program is described by Heller et al., 2017, Lam et al., (this issue), Lee et al., (this issue) and Ohnemus and Lam, 2015. The filter manifold was used to collect up to four 25 mm filters simultaneously on a third, un-metered flowpath of the McLane pumps: two 0.2 µm polycarbonate filters for analysis by STXM and two 0.2 µm polyethersulfone (PES) filters for X-ray Microprobe. Shipboard, the filter manifold was opened in an anaerobic chamber (Coy Labs) to prevent exposure of the sample to ambient oxygen, and

all sample processing occurred under a nitrogen-hydrogen (95% N_2, 5% H_2) atmosphere (the anaerobic chamber was vented within a self-built shipboard High Efficiency Particulate Arresting (HEPA) chamber). Filters were rinsed using N_2-sparged 18.2 MΩ·cm purified double distilled water (MilliQ) via vacuum pump to remove seasalts (the pump was located outside of the HEPA bubble with a line plumbed to the anaerobic chamber). Replicate filters were: (1) placed in acid-washed PetriSlides for X-ray microprobe analysis and archiving, and (2) placed in acid-washed microfuge tubes with 0.5 mL N_2-sparged MilliQ for STXM preparation. Prior to leaving the anaerobic chamber, all samples were sealed in mylar bags with an oxygen-free atmosphere. Sample packs were then frozen at -20˚C to reduce the kinetics of chemical oxidation.

2.1.2 Particulate Organic C (POC), Inorganic C (PIC), Mn (pMn), and Fe (pFe) Analyses

Size fractionated (1-51 µm; >51 µm) samples for bulk POC, PIC, pMn, and pFe analyses were collected on 142 mm filters connected to the two main, metered flowpaths of the McLane *in-situ* pumps. Sampling and analytical details are described in Lam et al., (this issue). Briefly, POC was determined from combustion in elemental analyzers, PIC was measured directly by coulometry, which is the measurement of CO_2 upon addition of weak acid. Particulate Mn and pFe were measured by high resolution inductively coupled plasma mass spectrometry (HR-ICP-MS) following a two-step total digestion in a strongly oxidizing solution followed by a strong mineral acid mixture on a hotplate. Bulk compositions are reported as the sum of the two size fractions, and represent particulate concentrations > 1 µm.

2.1.3 Sediment Core Collection

At Station 20, a sediment core was collected using a Royal Netherlands Institute for Sea Research (NIOZ) mono-corer, specifically designed to collect surface sediment samples with minimal disturbance of the sediment-water interface which was suspended from the ODF (Ocean Data Facility) CTD (conductivity, temperature, depth)-rosette for the final deep cast conducted at that station. In a shipboard cold room (4°C), the overlying seawater was syphoned off, down to ~0.5 cm above the 1-2 cm thick visible fluff layer. Then, the fluff layer was syphened off, being

careful not to resuspend the consolidated sediment, and solids were separated by centrifugation within hour of sediment core recovery. The pellet of fluff material was then frozen in the tip of the 50 mL polypropylene centrifuge tubes. Shore-based splitting of the fluff layer sample was accomplished by thawing the pellet and resuspending in pH purified water (Milli-Q water with a small volume of ultraclean NH_4OH), then removing representative sub-samples with a pipet while vortex mixing to maintain a homogeneous suspension." Prior to XANES analysis, fluff layer materials were separated from aqueous solution by 0.2 μm filtration. Sediment coring was not possible at Station 18 due to the very thin sediment cover at the site, so only data from Station 20 is reported here.

2.2 X-ray Absorption Spectroscopy

2.2.1 Scanning Transmission X-ray Microscopy

Water column samples from Station 18 and 20 were prepared in an anaerobic chamber for STXM analysis by defrosting and gently shaking the PC filter (stored in 0.5 mL of N_2-sparged MilliQ). Approximately 1 μL of the suspension was deposited onto a silicon nitride membrane (Silson Ltd.) and allowed to dry at ambient temperature in the glove bag. Imaging and C 1s and Fe 2p XANES spectroscopy were conducted at beamline 5.3.2.2, Advanced Light Source (ALS), Lawrence Berkeley National Laboratory, Berkeley, CA, USA (Kilcoyne et al., 2003). Samples were analyzed in a helium flushed microscope chamber. The transfer of the sample from the mylar packaging to the instrument resulted in approximately 30 s of exposure to ambient conditions. For Station 18 and 20 samples, we collected three different types of data: (1) transmission images covering sample areas from 1 mm^2 to 10 μm^2, (2) elemental maps for C and Fe, (3) C 1s and Fe 2p XANES spectra in point-scans, line-scans, or three dimensional "stacks" (a series of 2D images at different incident energies spanning the C and Fe absorption edges such that full XANES spectra can be extracted from each pixel of the composite stack of images) (e.g. Barber et al., 2017; Brandes et al., 2004; Chan et al., 2011; Chen et al., 2014; Toner et al., 2016, 2009a). Elemental maps reveal particle morphology and the location of C and Fe within particles. Carbon 1s XANES distinguishes between Corg and inorganic C (Cinorg), while Fe 2p XANES differentiates between reduced or oxidized Fe species. Data processing included

principle component analysis for the selection of groups of pixels having related spectral properties, pre-edge subtraction, post-edge normalization, and elemental optical density maps using the software *axis2000* (Hitchcock, 2016). Normalized spectra were compared to our C 1s and Fe 2p reference databases and literature for identification. Reference materials for C 1s and Fe 2p are published elsewhere (Brandes et al., 2010, 2004; Chan et al., 2011; Fenter et al., 2002; Sedlmair et al., 2012; Stöhr, 2003; Toner et al., 2009a; Urquhart and Ade, 2002).

2.2.2 X-ray Microprobe

The speciation of Fe in plume particles was measured using micro-focused XRF and Fe 1s μXANES spectroscopy at beamline 10.3.2 of the ALS with previously developed methods for marine particles (Breier et al., 2012; Lam et al., 2012; Marcus et al., 2004; Toner et al., 2012, 2016, 2014). All particles were analyzed on original polyethersulfone (PES; trademark SUPOR) filters and all sample preparation was conducted within positive pressure (N_2 or Ar) glove bags. The final step in sample preparation included application of a layer of sulfur-free mylar film (Premier Lab Supply TF-125-255) to limit exposure of the sample to ambient oxygen during analysis using the method established by Zeng et al., (2013). The monochromator was calibrated using an Fe foil XANES scan with the inflection point set to 7110.75 eV (Kraft et al., 1996). Micro-XRF and μXANES data were collected using a Canberra 7-element Ge solid-state fluorescence detector. Micro-XANES data were collected from 7012 to 7417 eV in quick-XANES mode with a single sweep of the monochromator lasting 30 s.

Data collection occurred in the following manner for each filter: (1) a large μXRF "survey" map with an area of approximately 1000 × 3000 μm^2, pixels of 6 × 6 μm^2, and incident energy of 10 keV was collected to measure the distribution of particles and elements on the filter; (2) "fine" μXRF sub-maps of approximately 100 × 100 μm^2, pixels of 3 × 3 μm^2, and incident energies spanning the Fe 1s absorption edge; and (3) Fe 1s point-XANES spectra.

Data processing for XRF maps included deadtime correction and plotting with beamline 10.3.2 software (Marcus et al., 2004). Data processing for the XANES spectra included deadtime correction, energy calibration, pre-edge subtraction, post-edge normalization, and linear least-

285 squares fitting with a reference database using beamline 10.3.2., *Athena*, and *SixPack* softwares
286 (Marcus et al., 2008, 2004; Ravel and Newville, 2005; Webb, 2005).
287
288 ***2.2.3 Bulk X-ray Absorption Spectroscopy***
289
290 For fine particles associated with the fluff layer, bulk C, Mn, and Fe 1s XANES spectra were
291 collected at the Canadian Light Source (CLS) in Saskatoon, Saskatchewan, Canada.
292
293 The bulk C 1s XANES were collected at the CLS High Resolution Spherical Grating
294 Monochromator (SGM) beamline. The sediment was applied to gold-coated silicon-chips as an
295 aqueous droplet under ambient temperature and atmosphere, allowed to dry, and placed in the
296 SGM vacuum sample-chamber. Sample analysis parameters were chosen to: (1) prevent photon-
297 damage to the sample, (2) collect data representative of the sample, and (3) improve signal-to-
298 noise through a series of fast (30-60 s) and non-overlapping point scans (Gillespie et al., 2015).
299 All experimental spectra were collected in fluorescence mode using an Amptek silicon-drift
300 detector positioned at 45 degrees. The incident beam, I_0 signal, was collected as scattered beam
301 from a blank gold-coated sample holder using a second Amptek detector positioned at 90
302 degrees. Individual spectra were curated, averaged, and normalized to I_0 using a custom script
303 prepared by Adam Gillespie in Igor Pro (Gillespie et al., 2014). Energy calibration, pre-edge
304 subtraction, and post-edge normalization were accomplished using *Athena* software (Ravel and
305 Newville, 2005). Spectra were compared to 13 carbonate mineral reference spectra provided by
306 Jay Brandes (Brandes et al., 2010).
307
308 The bulk Mn and Fe 1s XANES spectra were collected at the CLS Soft X-ray
309 Microcharacterization Beamline (SXRMB). The sediment was applied as a dry powder to
310 double-sided C tape and adhered to a copper sample plate under ambient temperature and
311 atmosphere, and placed in the SXRMB vacuum sample-chamber. The monochromator was
312 calibrated using an Fe foil XANES scan with the inflection point set to 7110.75 eV (Kraft et al.,
313 1996). All experimental spectra were collected in fluorescence mode using an Amptek silicon-
314 drift detector positioned at 45 degrees, with I_0 collected simultaneously in an ion chamber. Data
315 processing for the XANES spectra consisted of I_0 normalization, energy calibration, pre-edge

subtraction, post-edge normalization, and linear least-squares fitting with a reference database using beamline 10.3.2., *Athena*, and *SixPack* softwares (Marcus et al., 2008, 2004; Ravel and Newville, 2005; Webb, 2005). Linear combination fitting of Mn 1s XANES with reference spectra in the energy range of 6500-6650 eV was accomplished using laboratory synthesized standards: birnessite ($KMnO_2$), δ-MnO_2, manganite (γ-MnOOH), Mn_2O_3 (bixbyite), and Mn_3O_4 (hausmannite) (Bargar et al., 2000; Villalobos et al., 2003). The Fe 1s XANES spectrum was fit using linear combinations of 70 reference spectra in the energy range of 7110-7400 eV (Marcus et al., 2008).

3. Results

3.1 Bulk Chemistry of Plume Particles

Concentration profiles for total (> 1 μm) POC, PIC, pFe, and pMn from Stations 17, 18, and 20 are shown in Figure 1. Station 17 is upstream of the ridge, Station 18 is at the ridge crest, and Station 20 is downstream from the ridge.

There is an increase in pFe and pMn concentrations at Station 18 and 20 compared to Station 17 at mid-plume depth, and compared to the water column above (above plume background). The enriched particulate metal concentrations, centered at ~2500 m water depth, coincide with the SEPR hydrothermal plume (Fitzsimmons et al., 2017; Lam et al., this issue; Lee et al., this issue). At Station 18, the above plume background pFe and pMn concentrations are 0.56 nM and 0.11 nM, respectively (2200 m water depth). At the mid-plume depth of Station 18 (2450 m water depth), the pFe and pMn concentrations are two orders of magnitude higher 44.2 nM and 5.2 nM, respectively. At Station 20, the pFe and pMn concentrations are lower by still quite high at the mid-plume (2550 m; 28.9 nM pFe and 6.38 nM pMn) are also enriched over the above plume background (2200 m; 0.76 nM pFe and 0.12 nM pMn). The low Station 17 pFe and pMn concentrations at mid-plume depth (2500m; 0.307 nM pFe and 0.075 nM pMn) suggest the increase is not from lateral advection from stations east of the plume.

At the mid-plume depth of Station 18, there is a measurable increase in total POC concentration over background (above plume background and mid-plume depth of Station 17) concentrations

that is consistent with plume-generated POC or sorption of dissolved OC (DOC) onto mineral surfaces (Lam et al., this issue). A small decrease in total PIC concentration in the plume (Station 18 and 20) is likely due to enhanced aggregation and removal in the plume (Lam et al., this issue). The bulk chemistry is further discussed in Lam et al., (this issue) and Lee et al., (this issue).

3.2 Bulk Chemistry of Station 20 Sediment Fluff

Sub-samples of the fine fluff layer materials from Station 20 were examined by bulk C 1s, Mn 1s, and Fe 1s XANES.

The bulk C 1s XANES spectrum (Figure 2a) was compared to that 13 carbonate minerals and was most consistent with calcite (Brandes et al., 2010). Brandes et al., (2010) reports that the intensity of the main peak for the carbonate minerals varies due to crystal orientation (Brandes et al., 2010; see Figure 2a for a calcite example). Our fluff sample is composed of randomly oriented crystals (whole mount, drop coat preparation), so the main peak height has intermediate intensity relative to the standards. Although calcite spectra are very similar to aragonite, from our STXM and XRF maps (Figure SI 1-2), we know that coccoliths and foraminifera are common in this sample, and therefore, the phase identification is calcite (de Vargas et al., 2007).

The bulk Fe 1s XANES spectrum (Figure 2b) was fit using linear combinations of 70 reference spectra in the energy range of 7110-7400 eV (Marcus et al., 2008). The best fit to the data was a three-component fit composed of 70 atom % marine Fe(III) oxyhydroxide ("biogenic iron oxyhydroxide"; Toner et al., 2009b), 15 atom % augite (inosilicate), and 15 atom % roedderite (cyclosilicate).

The bulk Mn 1s XANES spectrum (Figure 2c) was fit using linear combinations of reference spectra in the energy range of 6500-6650 eV: birnessite ($KMnO_2$), δ-MnO_2, manganite (γ-MnOOH), Mn_2O_3 (bixbyite), and Mn_3O_4 (hausmannite) (Bargar et al., 2000; Villalobos et al., 2003). The best fit was a one-component fit with δ-MnO_2. The δ-MnO_2 standard is a synthetic layer-type Mn oxide with hexagonal-in-sheet symmetry and an average oxidation number of 4.02 ± 0.02 (Villalobos et al., 2003).

3.3 Particle-by-Particle Chemistry of Plume

Samples from above (above plume background), within (top, middle, and bottom), and below (near bottom background) the well-defined plume (Jenkins et al., this issue), as well as fluff layer, were analyzed by STXM and the X-ray microprobe (Table 1). STXM was used to visualize particle morphology and intra-particle texture, as well as C and Fe chemistry through C 1s and Fe 2p XANES. The X-ray microprobe was used to collect Fe 1s XANES. Together, these two techniques allow us to visualize intra- and inter-particle characteristics, and to measure Fe and C chemistry.

3.3.1 Carbon 1s and Fe 2p Scanning Transmission X-ray Microscopy and X-ray Absorption Near Edge Structure Spectroscopy

Images, total C maps, and total Fe maps for particles collected above, within, and below the hydrothermal plume at Stations 18 and 20, as well as the fluff layer from Station 20, are displayed in Figures 3 and 4 (additional data in Supplemental Information, SI, Figures S3-S10).

Carbon 1s spectra were collected on particles from above, within, and below the hydrothermal plume at Stations 18 and 20, as well as sediments from Station 20 (Figures 3j, 4p, S3n, S4u, S5r, S6k, S7v, S8l, S9l, S10j). Spectra were collected from sample areas thin enough to have good X-ray transmitting properties. Principal component analysis (PCA) of the spectral datasets generated by STXM was used to investigate intra-particle C chemistry. Often, the PCA components were composed of spectra having similar chemistry but with different degrees of saturation based on variations in sample thickness. When particles had uniform C chemistry, a single representative spectrum was chosen for analysis and display.

Tables 2 and 3 report the initial, primary, and secondary peak positions and C bonding information for representative C 1s XANES spectra for each Station. Specific peaks and spectral shapes are used as a fingerprint to identify C compounds in each sample:

(1) Within the plume at Station 18 and 20, the C chemistry of samples was most consistent with aliphatic chained compounds that contained alkene or aromatic features (Brandes et al., 2004). Occasionally, carbonyl or organic acid features were observed. These characteristics are observed in many organic molecules, such as ligands, as well as DOC and POC (Boiteau et al., 2016; Golchin et al., 1994; Weishaar et al., 2003).

(2) At Station 18, the above plume background particles typically yielded spectra with alkene/ring, carbonyl, and alcohol moieties (Figure 3a, j; Brandes et al., 2004; Fenter et al., 2002; Sedlmair et al., 2012). These characteristics are consistent with fatty acids, commonly found in cell membranes/walls. Unlike the plume samples, the above plume background initial peak has higher intensity relative to particles located within the plume and does not return to the baseline before increasing to the primary peak (Figure 3j; Table 2).

(3) At Station 20, the near bottom background particles typically yielded spectra most consistent with proteinaceous material when compared to our reference spectra and the literature (Brandes et al., 2004; Chan et al., 2011). The spectra are consistent with aromatic/olefinic bonds in amino acids and amide-linked carbonyl groups (Brandes et al., 2004). These spectra and associated images indicate that the near bottom background particles are rich in microbial biomass, including intact, free-living cells.

(4) The fluff layer at Station 20 contains two distinct spectral signatures. The first is a Corg signal associated with a carbonyl moiety and is consistent with the lipid standard from our reference database (Chan et al., 2011). The second C signature contains a combined Corg and Cinorg signals, with the Cinorg signal contributed by calcite ($CaCO_3$; Brandes et al., 2010). The Cinorg is observed in coccolith fragments that have settled out of the upper water column (de Vargas et al., 2007; Figures 4m,n, S10). The biofilm-like, lipid-rich materials observed in the fluff layer appear to be unique to the benthic region, when compared with near bottom background, plume, and above plume background samples.

Iron 2p XANES spectra for particles within the hydrothermal plume at Stations 18 and 20 are displayed in Figure 5, and are consistent with Fe(III) oxyhydroxides, which have one distinctive peak at 709.6 eV. While the Fe 2p XANES are sensitive to Fe(II) versus Fe(III), and Fe(II)-bearing silicates versus Fe-sulfides, it is rather insensitive to the different Fe(III) oxyhydroxide

forms (Toner et al., 2009b; von der Heyden et al., 2012). These Station 18 and 20 spectra are consistent with an oxidized plume dominated by Fe(III)-bearing particles, and no instances of fine grained Fe-sulfides were observed by STXM.

3.3.2 Microprobe Iron 1s X-ray Absorption Near Edge Structure Spectroscopy

Particulate Fe speciation, as described by Fe 1s μXANES, is reported in Figure 6 for Station 18 and 20. Approximately 10-20 Fe 1s μXANES spots were examined for each sample from within the near-field hydrothermal plume (Table 1). As described for bulk Fe 1s XANES, the data were fit using linear combinations of reference materials. Those fit results were binned post-fitting into the following broad categories based on the chemistry of Fe, the geologic setting, and the relative sensitivities of Fe 1s μXANES into different Fe-bearing phases: (1) Fe(III)-oxyhydroxides and -organics; (2) Fe(III) phyllosilicates; (3) Fe(II) oxides, salts, and glasses; (4) Fe sulfides; (5) silicates; and (6) native Fe. While any of these particle types could be transported from elsewhere (allochthonous), several of these categories represent materials that can readily form within plumes (autochothonous). The two separate categories for silicate minerals, “Fe(III) phyllosilicates” and “silicates”, were chosen to represent the fact that phyllosilicates may form within the plume while nesosilicates, inosilicates, tectosilicates, cyclosilicates (hereafter “silicates”) are unlikely to form within the plume. “Native” Fe is an Fe(0) or metallic form which, in general, is considered to be a ship/surface ocean contaminant.

Compared to background, plume particles from Stations 18 and 20 had 60 % or greater, on a per atom basis, Fe(III) oxyhydroxide materials, with ferrihydrite-like phases being the most common best-fit to the data (Table 4 and Figure S11). Iron(III)-bearing phyllosilicates contributed an additional ~ 5 - 30 % of the particulate Fe(III). The high percentage of Fe(III) detected with microprobe Fe 1s μXANES is consistent with the STXM-generated Fe 2p and bulk Fe 1s XANES results (Figures 5 and 6). Non-sulfide, Fe(II)-bearing phases contributed ~ 5 - 20% of the Fe, while silicates represented minor contributors of Fe to the plume. Iron-bearing sulfides were present in trace quantities in the plume and were detected in two of our samples at 0.1 % and 0.4 % Fe (per atom basis). No measurable difference in particulate Fe speciation between Station 18 and 20 at plume depths was observed.

The near bottom background and fluff layer at Station 20 share overall Fe speciation characteristics: high Fe(III) oxyhydroxides (> 80 %) with phyllosilicates, silicates, and Fe(II) in the range of ~ 1 – 14 % each (Figure 6; Table 4). However, the near bottom background have trace quantities of Fe sulfide (0.3 %), while no Fe sulfides were detected within the fluff layer at Station 20. The pFe speciation in the near-field, near bottom background, and fluff layer were quite similar to but more oxidized than the overlying plume (i.e. more Fe(III) and less Fe(II)).

The above plume background sample exhibited the greatest diversity of pFe speciation with ~ 60 % Fe(III) oxyhydroxide and ~ 10 % each of Fe(III) phyllosilicates, Fe sulfide, native Fe, and Fe(II). Native Fe is considered to be a contaminant from the ship, while Fe sulfides could be attributed to the production of reduced sulfur compounds created by plankton in the upper water column (Durham et al., 2015; Ksionzek et al., 2016; Ohnemus et al., 2016). Recently, Ohnemus et al. (2016) observed acid volatile sulfide (AVS) concentrations in the euphotic zone overlaying the SEPR hydrothermal plume which they attributed to the phytoplankton production of reduced sulfur. Unlike the plume, near bottom background, and fluff layer, no silicates were detected in the above plume background at this depth. While the diversity of Fe phases was greater in the above plume background than the plume, the overall pFe concentrations in the above plume background were ~ 60 times lower than the plume (Figure 3).

4. Discussion

4.1 Plume Particle Morphology and Chemistry

Overall, there is much diversity in particle morphology and chemistry in the near-field SEPR hydrothermal plume. However, several trends are observed from samples collected above-plume, within-plume (top, middle, and bottom), below-plume, and at the fluff layer. In general, materials collected within the plume are characterized by strong C- and Fe-enrichment, a high degree of co-location between the two elements, and organic-rich materials (as previously observed for plumes of the EPR 9-10˚N area; Toner et al., 2009a) (Figures 3d-i, 4a-i, S4, S5, S6, S7, S8). For all water column samples (above plume background, within-plume, and near bottom

502 background), the C chemistry is most consistent with Corg compounds, while the fluff layer at
503 Station 20 is a mixture of Corg and Cinorg.
504
505 The plume-top particles from Station 20 are an exception to the overall morphology trends
506 within the plume. Particle morphologies at this location indicate a mixture of plume derived
507 materials and sinking POC from the overlying water column (Figure 4a-c, S6). Cell wall
508 remnants and diatoms have been reported to preserve POC through the water column and contain
509 distinct branching or patterned morphologies (Abramson et al., 2009; Brandes et al., 2004),
510 which can be seen in Figure S6i-j. Particles also contain C-rich matrices that have been observed
511 previously in hydrothermal plumes (Toner et al., 2009a). However, while the plume-top particles
512 are C-rich, Fe element maps indicate particles are either depleted in or Fe-poor. These
513 observations suggest that the plume-top particles are a combination of above plume background
514 and in-plume materials.
515
516 The in-plume particles are distinct from the marine particles sampled above and below the plume
517 in terms of relative Fe:C, particle morphology, and degree of co-location of Fe and C in particles.
518 The above plume background sample from Station 18 is enriched in C and depleted in Fe relative
519 to the in-plume particles (Figure 3a-c, S3). Samples from the near bottom background, the water
520 depth below the well-defined ^{3}He plume (Jenkins et al., this issue), are Fe-rich particles coated
521 by organics and are distinct from plume samples with regards to morphology and chemistry
522 (Figure 4j-l, S9). For example, in some cases, the near bottom background particles are microbial
523 cells (Figures 4k, S9b, e, and g). In the Station 20 fluff layer, C and Fe are both detected.
524 However, the pattern of co-location of these elements is different from that observed in the
525 plume (Figures 4m, n, o, S10). Iron is concentrated in coccolith fragments (Cinorg), while Corg
526 is dominated by lipid-rich material. The lipid-like materials are potentially produced by
527 microbial processing of hydrothermal and/or upper water column inputs to the sediments. These
528 specific elemental correlations, and particle morphologies and chemistries are unique to the fluff
529 layer and not observed in any of the water column samples.
530
531 The C chemistry within the plume is distinct from that of the above plume background and near
532 bottom background. Within the plume at Station 18 and 20, the C 1s XANES spectra are

characterized by plume particles containing aliphatic chains or carbonyl groups (Table 2). All spectra contained an initial peak at ~285 eV; associated with either an unsaturated chain or aromatic ring. A primary peak between 287.7-288.6 eV was observed and is consistent with acarbonyl moiety (Brandes et al., 2004). At Station 20, there was increasing aliphatic character in the in-plume material.. All spectra at Station 20 contain carbonyl moieties, with the top of the plume containing the strongest signal of that type (Fig. 4p; Table 2) (Brandes et al., 2004).

4.2 Sources of Particulate Organic Carbon to the Plume

Sources of POC to the non-buoyant plume could include: (1) upstream contributions from laterally advecting deep ocean water and settling particles from the upper water column; (2) sub-seafloor processes such as microbial activity and abiotic synthesis; (3) mixing with deep ocean water during dispersion; (4) entrainment into the buoyant plume of materials from vent biota, sediments, and deep ocean waters; (5) biological activity within the plume; and (6) transfer of DOC to POC within the plume via adsorption (to solids). Source 1 contributes to background POC at plume depth but does not account for the POC profile observed at Station 18 (Figure 1; upstream POC concentrations at Station 17 are low at plume depth). Due to dilution in the buoyant plume (ca. 1:10,000 vent fluid:seawater), sub-seafloor contributions to the POC in the non-buoyant plume (i.e. Source 2) at Stations 18 and 20 should be negligible. The particle characteristics and morphologies of the plume-top particles at Station 20 provide evidence for some mixing with overlying water (i.e. Source 3), but the POC profile indicates that the waters above the plume are lower in POC than the plume so are not expected to be a major source of POC to the plume (Figure 1). These observations are supported by POC profiles (Figure 1) that show clear enhancements of POC concentrations at plume depths relative to above plume background, near bottom background, and Station 17 (up current of the ridge) values and are discussed in detail in Lam et al., (this issue). Overall, our data are most consistent with sources 4-6, and these are discussed below.

With sub-seafloor, and advected/settling sources of POC to the plume rejected as major contributors of plume Corg, the main sources must be entrainment of near-vent material, biological activity within the plume and/or DOC sorption. Entrainment of POC into the buoyant

plume (Bennett et al., 2015, 2013, 2011b; Breier et al., 2012; Dick et al., 2013; Jiang and Breier, 2014; Olins et al., 2017) and the production of POC within non-buoyant plumes (Bennett et al., 2015, 2013, 2011a, 2011b) have been identified as major processes active at vent fields. High POC concentrations have been reported at EPR 9˚50'N for the dispersing plume, similar to the features we observe for Stations 18 and 20 at SEPR (Figure 1) (Bennett et al., 2011b).

Within the plume at Stations 18 and 20, we observe that the dominant pFe species is Fe(III) oxyhydroxides (Figure 6). Given a conservative surface area for Fe(III) oxyhydroxides ($100 m^2/g$) and a Corg sorption ratio of 0.76 mg/m^2, we would predict approximately 27 nM of DOC could be predicted adsorbed to plume particles (Keil et al., 1993; Lam et al., this issue). This sorption of DOC to mineral surfaces could result in the enrichment in the total POC observed within the plume, and would be an additional explanation of the feature observed in Figure 1.

We observe that Corg- and Fe(III)-rich particles at Stations 18 and 20 have similar morphologies, textures, C distribution, Fe distribution and mineralogy in the plume (Figures 3, 4, 6, S4, S7). While transport of vent-derived material off-axis on this length scale is in agreement with prior work at this site (Feely et al., 1996), the SEPR non-buoyant plume is likely a coalescence of materials from many vents in the vicinity of our sampling locations. Therefore, a conceptual model comprising only *de novo* plume particle formation at Station 18 and advection of those materials to Station 20 may be an over-simplification. However, estimates of plume ages using short- and medium-lived radium (Ra) isotopes indicate that materials are progressively older downstream in the plume: at Stations 18 and 20, the in-plume materials were ~1 month and 2.4 - 5.5 years old, respectively (Kipp et al., this issue). This suggests that some of the plume particles at Station 20 are the result of 80+ km of transport from Station 18 and vent sites further south.

Using the conceptual model of in-plume transport of POC from Station 18 to 20, we can further evaluate POC entrainment into or production within the SEPR plume through a comparison of particle morphology and C chemistry of other near-vent systems along the EPR. The SEPR mid-plume POC at Stations 18 and 20 bears morphological resemblance to particles collected within

~ 250 m of EPR 9-10˚N (Breier et al., 2012, 2009, Toner et al., 2012, 2009a). However, the plume POC and Fe chemistries are different between the two sites. Specifically, non-buoyant plume and settling plume particles are both rich in proteinaceous material at EPR 9-10˚N, which is taken as evidence for fresh vent biomass inputs (Breier et al., 2012; Toner et al., 2009a). At Station 18, some proteinaceous signatures are also observed (Figure 3j) but they are less common at Station 20 (Figures S6-10). This suggests that near-vent Corg inputs could be important for the SEPR, but that certain POC pools are lost during transport through biogeochemical alteration and/or differential settling. Whether the mechanisms of alteration are biological, chemical, physical, or some combination, the trend of particle alteration within the plume appears to continue past Station 20. Fitzsimmons et al. (2017) recently reported that plume particle morphology and chemistry continue to change between Stations 20 and 21 of the EPZT.

4.3 Evidence for a Sulfur-Depleted Plume

Past work at the SEPR revealed variable pS (> 0.4 μm) concentrations in non-buoyant plume particles from 13º33’ to 18º40’S (Feely et al., 1996): the mean Fe:S and mean pS concentration were reported as 13.72 ± 19.96 nM (0.44 ± 0.64 μg / L) and 1375 ± 873.2 nM (44.1 ± 38 μg / L), respectively. Feely et al. (1996) used pFe and pS concentrations, nephelometer data, and transmission electron microscopy to conclude that the plumes were Fe-rich and S-depleted north of 17º20′ S. Overall, the bulk Fe 1s, microprobe Fe 1s, and STXM-Fe 2p XANES data sets presented in this contribution are consistent with a near-field environment that is dominated by oxidizing conditions and depleted in Fe-S bearing minerals. The depleted S status of the plume could reflect several different properties of the vent and plume at this location:

(1) The vented fluids at SEPR near 15ºS could have low pS concentration. This would be consistent with the work of Feely et al. (1996). At this time, the vent fields and vent fluid characteristics for this region of the SEPR are not known, so the Fe:S in fluids contributing to the plume cannot be assessed directly at this time.

(2) The particle size of S-bearing materials could be less than the 0.2 µm filter used in this study, and be part of the nano-particulate or colloidal pool (e.g. Yücel et al., 2011). However, this is unlikely given the isotopically heavy values observed in the SERP dFe plume (Fitzsimmons et al., 2017). When Fe-sulfides precipitate in the plume, they carry an isotopically light signature, regardless of the particulate size fraction (nano or macro).

(3) The pS could be preferentially removed from the plume by oxidation or settling processes during the ~ 1 month in-plume residence time of particles at Station 18 and 2.4-5.5 years at Station 20 (Kipp et al., this issue).

4.4 Characteristics of Settling Plume Material

For the Station 20 fluff layer, the STXM results indicate that both Corg (POC) and Cinorg (PIC) bearing phases are present (Figure 4, S10). The bulk C 1s XANES spectrum confirms the STXM observations and shows a Cinorg:Corg of approximately 10:1 based on normalized absorption intensity. The inputs of materials to the sediments at Station 20 are from the upper water column and overlying hydrothermal plume. The PIC:POC at the mid-plume (depth of 2500 m) is approximately 0.25 (Figure 1), so the plume is enriched in Corg (relative to Cinorg) in comparison to the fluff layer. The mean photic zone PIC:POC in the small size fraction (SSF; 1-51µm) is 0.04 ± 0.02, while the large size fraction (LSF; > 51 µm) is 0.14 ± 0.29 (Lam et al., this issue), so the water column is greatly enriched in Corg. The PIC:POC is known to generally increase with water depth as POC remineralizes faster than PIC dissolves in the water column. The PIC:POC in sediments reflects the tendency of POC to be respired while PIC tends to be preserved (i.e. the sediments and entire water column at Station 20 are above the calcite saturation horizon). Overall, the particle morphology and C chemistry (as measured by XANES) of the fluff layer is different from the above plume background, plume, and near bottom background measured for this study. These findings are consistent with the bulk PIC-POC values in that the Corg inputs to the fluff layer appear to be extensively remineralized and altered (Sayles et al., 2001; Ziervogel and Forster, 2005).

The STXM, microprobe, and bulk XANES results are consistent with chemically oxidizing conditions in the fluff layer at Station 20. The Fe and Mn mineralogy is dominated by Fe(III) oxyhydroxides and Mn(IV) oxides (Figure 2). While the microprobe Fe 1s XANES analysis did detect Fe-sulfide particles in the near bottom background and two plume samples, no Fe-sulfides were detected in the fluff layer by any of our methods (Figure 6).

4.5 Particle Formation and Transport Characteristics

Within the plume at Station 18, the spatial correlation of Fe, Mn, and Ca in particles is not strong. For example, in the plume at Station 18, we observe particles rich in only Fe, rich in only Mn, rich in only Ca, as well as binary and tertiary combinations of the three elements (red, green, blue, yellow, and white particles in XRF maps, Figure S12). However, if a comparison of Station 18 and 20 is made at mid-plume, it appears that a separate population of Mn-rich particles is emerging (green particles in XRF maps, Figure S13). Fitzsimmons et al. (2017), Lam et al. (this issue), and Lee et al. (this issue) also report different behavior for pMn and pFe in the SEPR plume. Lee et al. (this issue) noted the sinking of LSF aggregates from the plume for both pFe and pMn at Station 18 and 20. However, pFe was observed to partition preferentially into the SSF while pMn was distributed equally between the LSF and SSF at Station 18 and 20. This would imply different oxidation, precipitation, and/or aggregation dynamics for these two elements in the near field. Fitzsimmons et al. (2017) noted that both pFe and pMn removal were consistent with first order kinetics from Station 20 westward. However, the pMn and $^{3}He_{xs}$ plumes did not settle gravitationally in their westward extension while the pFe (and dFe) plume did. Fitzsimmons et al. (2017) hypothesized that the far-field pMn behavior might be caused by Mn-oxidizing bacteria within the SEPR plume.

Recent research has mainly focused on exploring possible transport mechanisms for pFe in hydrothermal plumes (Bennett et al., 2011a, 2008; Butler, 2005; Fitzsimmons et al., 2017, 2014; Sander and Koschinsky, 2011; Toner et al., 2009a; Yücel et al., 2011). However, many aspects of those proposed mechanisms for Fe should also apply to Mn. Iron and Mn are both redox active transition metals whose reduced divalent states (Fe^{2+}, Mn^{2+}) are soluble in seawater (Emerson, 2000; Tebo et al., 2004). These elements also share a tendency for the oxidized

trivalent states (Fe^{3+}, Mn^{3+}) to form strong complexes with organic ligands and precipitate to form sparingly soluble oxides, hydroxides, and oxyhydroxide minerals (Cornell and Schwertmann, 2003; Hem and Lind, 1983; Kostka et al., 1995; Post, 1999; Sander and Koschinsky, 2011; Trouwborst et al., 2006; Wu and Luther, 1995). Manganese has an additional 4+ state that is common in Earth surface environments as sparingly soluble Mn(IV) oxides (Post, 1999). The Fe- and Mn-bearing minerals formed in aqueous/soil/sediment systems tend to be finely grained, often nanoparticulate, with high (bio)geochemical reactivity (e.g. Brown et al., 1999; Emerson et al., 2010; Navrotsky et al., 2008; Nealson et al., 1989). These two elements also have an essential difference that bears strongly on their behavior in oxygenated seawater: abiotic Fe^{2+} oxidation by dissolved oxygen is rapid, while Mn^{2+} oxidation is slow without a catalyst (such as microbes or mineral surfaces; e.g. Field and Sherrell, 2000; Nealson et al., 1989). While we can expect certain particle properties to affect pFe and pMn transport similarly (size, density), microbial activity and surface catalysis could have a larger role in pMn transport characteristics.

Microbial oxidation of Mn that leads to the production of pMn in hydrothermal vent systems is well established, especially for the Guaymas Basin and Juan de Fuca Ridge. The evidence ranges from transmission electron microscopy, to shipboard kinetic experiments, to meta-transcriptomic tracking of Mn(II) oxidation genes during entrainment of microbial populations in the Guaymas Basin plumes (Cowen et al., 1986; Dick et al., 2006; Dick and Tebo, 2010; Kadko et al., 1990; Mandernack and Tebo, 1993). Based on all that is known about Mn chemistry in natural systems, we expect that homogeneous Mn oxidation will proceed more slowly than Fe oxidation unless microbial or surface catalyzed oxidation processes are occurring. Microbial oxidation places the solid-phase Mn(III, IV) products of that reaction in close proximity to cells and cellular exudates. It has been demonstrated through microscopy that Mn oxidation in the laboratory and in nature for a wide variety of microorganisms creates microbe-mineral composite particles (e.g. Cowen et al., 1986; Santelli et al., 2011; Tebo et al., 2004; Toner et al., 2005). Therefore, it is reasonable to assume that pMn in the EPZT plume has this composite character.

We have demonstrated through direct observation that the pFe of the EPZT plume also consists of organic-inorganic composites (this contribution; Fitzsimmons et al., 2017). Why then do we

observe different settling behaviors between pFe and pMn over short and long transport distances? We propose that the main difference in settling is based on the timing and in-plume location of the interactions between the metal and Corg. These differences in particle formation are created by the changes in rate and mechanism of oxidation for Fe and Mn. Therefore, in our low-S SEPR plume, Fe oxidizes rapidly to form Fe(III)oxyhydroxides. This process occurs within the buoyant and early non-buoyant plume and is likely complete within hours-days (Field and Sherrell, 2000). The composite nature of the pFe we observe suggests physical aggregation of Fe(III)oxyhydroxides with entrained Corg. Particles with those characteristics persist in the non-buoyant plume for 80+ km. However, we do have evidence that the particles change with greater transport time so the pFe must be subject to physical, chemical, or biological alteration (Fitzsimmons et al., 2017). These alteration processes may ultimately lead to particles with a size and density that allows a gradually settling pFe plume on a time scales of decades (Fitzsimmons et al., 2017).

In contrast to Fe, homogeneous Mn oxidation and particle formation should be slow in seawater. In the near-field, where dMn concentrations are high, microbial oxidation may cause initial oxidation and precipitation events through entrainment of active Mn-oxidizer populations (Bargar et al., 2005; Campbell et al., 1988; Dick et al., 2006; Hem, 1981; Hem and Lind, 1983; Johnson et al., 2016; Kessick and Morgan, 1975; Tebo et al., 2004; Webb et al., 2005). However, at high dMn concentrations, abiotic auto-oxidation/autocatalysis of Mn(II) by Mn(III, IV) phases could be a more important contributor to near-field particle growth (Hem, 1981; Kessick and Morgan, 1975). In this scenario, the particles could grow quickly, be combinations of Mn(II), Mn(III), and Mn(IV) reflecting a variety of possible reaction pathways (Hem and Lind, 1983; Johnson et al., 2016; Webb et al., 2005), and partition into the rapidly settling LSF as observed by Lee et al. (this issue). While we might expect the resulting pMn in the far-field plume to suffer the same fate as pFe (i.e. alteration and settling) the dilute conditions of the far-field plume may favor microbial Mn oxidation (Bargar et al., 2005). Any alteration of pMn that occurs within the far-field plume does not appear to change the overall neutral buoyancy of the pMn particle population (Fitzsimmons et al., 2017; Lee et al., this issue): perhaps because neutral buoyancy is a selective advantage to the Mn oxidizing microorganisms (e.g. dispersal, optimal dMn concentration). This is an area ripe for further investigation.

5. Conclusions

In this study, we have explored the hypothesis that Corg contributes to the export of hydrothermally sourced pFe over long distances into the interior of ocean basins (Fitzsimmons et al., 2017; Toner et al., 2009a; 2012). Through a suite of synchrotron X-ray microscopy, microprobe, and spectroscopy techniques, we have observed that in the non-buoyant hydrothermal plume at 15°S on the EPR, near-field plume particles are composites of mineral and biological materials that are dominated by Fe(III)-bearing oxyhydroxide phases but are also rich in Corg. The profiles for pFe and POC at background Station 17 (upstream of the ridge axis), and at Stations 18 (ridge axis) and 20 (83 km down-plume away from the ridge axis) all indicate that the inputs of both Fe and Corg to the dispersing plume are dominated by hydrothermally derived materials. The Fe is contributed by vent fluids directly, while the Corg is entrained from the near-vent ecosystems, sorbed to hydrothermal particles within the plume, or due to *in-situ* production associated with microbial activity within the plume. The particulate Fe(III)-Corg associations we observed in the non-buoyant plume extending out to 100 km off-axis from the ridge crest at SEPR are consistent submersible-based observations made previously in the near-field, no greater than 100 m from sites of active venting at the 9°N EPR site (Breier et al., 2012; Toner et al., 2009a). The commonality of processes revealed in this contribution demonstrates the export of hydrothermal pFe to the ocean interior is indeed facilitated through an association with Corg in dispersing non-buoyant plumes.

Acknowledgments

We thank captain and crew of *R/V Thomas G. Thompson* and Co-Chief Scientist James Moffett for supporting our research during the EPZT GP16 cruise. This research was supported by grants from the National Science Foundation to BMT (OCE-1232986), PJL (OCE-1518110), CRG (OCE-1235248), and RMS (OCE-1234827). We thank Sirine Fakra and Matthew Marcus, beamline scientists at the Advanced Light Source (ALS) 10.3.2, and David Kilcoyne, beamline scientist at ALS 5.3.2.2 for their mentorship, patience, and guidance in STXM and X-ray microprobe; Adam Gillespie, Tom Regier, and James Dynes, beamline scientists at the Canadian Light Source (CLS) SGM, and Yongfeng Hu, Aimee MacLennan, and Qunfeng Xiao, beamline scientists at the CLS SXRMB for their mentorship, patience, and guidance in bulk XANES

measurements; Brandi Cron Kamermans and Rebecca Sims for support in beamtime data collection; Andy Scobbie, Thor Sellie, Brandi Cron Kamermans, Rebecca Sims, Michael Ottman, Sofia Oufqir, and Reba VanBusekom for cruise preparation support; and James Brandes for sharing carbon XANES standard spectra for carbonate minerals. The Advanced Light Source is supported by the Director, Office of Science, Office of Basic Energy Sciences, of the U.S. Department of Energy under Contract No. DE-AC02-05CH11231. Research described in this paper was performed at the Canadian Light Source, which is supported by the Canada Foundation for Innovation, Natural Sciences and Engineering Research Council of Canada, the University of Saskatchewan, the Government of Saskatchewan, Western Economic Diversification Canada, the National Research Council Canada, and the Canadian Institutes of Health Research.

References

Abramson, L., Wirick, S., Lee, C., Jacobsen, C., Brandes, J.A., 2009. The use of soft X-ray spectromicroscopy to investigate the distribution and composition of organic matter in a diatom frustule and a biomimetic analog. Deep. Res. Part II Top. Stud. Oceanogr. 56, 1369–1380. doi:10.1016/j.dsr2.2008.11.031

Adams, D.K., Mcgillicuddy Jr, D.J., Zamudio, L., Thurnherr, A.M., Liang, X., Rouxel, O., German, C.R., Mullineaux, L.S., 2011. Surface-Generated Mesoscale Eddies. Science (80-.). 332, 580–583. doi:10.1126/science.1201066

Barber, A., Brandes, J., Leri, A., Lalonde, K., Balind, K., Wirick, S., Wang, J., Gélinas, Y., 2017. Preservation of organic matter in marine sediments by inner-sphere interactions with reactive iron. Sci. Rep. 7, 366. doi:10.1038/s41598-017-00494-0

Bargar, J.R., Tebo, B.M., Bergmann, U., Webb, S.M., Glatzel, P., Chiu, V.Q., Villalobos, M., 2005. Biotic and abiotic products of Mn(II) oxidation by spores of the marine Bacillus sp. strain SG-1. Am. Mineral. 90, 143–154. doi:10.2138/am.2005.1557

Bargar, J.R., Tebo, B.M., Villinski, J.E., 2000. In situ characterization of Mn(II) oxidation by spores of the marine Bacillus sp. strain SG-1. Geochim. Cosmochim. Acta 64, 2775–2778. doi:10.1016/S0016-7037(00)00368-9

Bennett, S.A., Coleman, M., Huber, J.A., Reddington, E., Kinsey, J.C., McIntyre, C., Seewald, J.S., German, C.R., 2013. Trophic regions of a hydrothermal plume dispersing away from

an ultramafic-hosted vent-system: Von Damm vent-site, Mid-Cayman Rise. Geochemistry, Geophys. Geosystems 14, 317–327. doi:10.1002/ggge.20063

Bennett, S.A., Dover, C. Van, Breier, J.A., Coleman, M., 2015. Effect of depth and vent fluid composition on the carbon sources at two neighboring deep-sea hydrothermal vent fields (Mid-Cayman Rise). Deep. Res. Part I Oceanogr. Res. Pap. 104, 122–133. doi:10.1016/j.dsr.2015.06.005

Bennett, S.A., Hansman, R.L., Sessions, A.L., Nakamura, K. ichi, Edwards, K.J., 2011a. Tracing iron-fueled microbial carbon production within the hydrothermal plume at the Loihi seamount. Geochim. Cosmochim. Acta 75, 5526–5539. doi:10.1016/j.gca.2011.06.039

Bennett, S.A., Statham, P.J., Green, D.R.H., Le Bris, N., Mcdermott, J.M., Prado, F., Rouxel, O.J., Damm, K. Von, German, C.R., 2011b. Dissolved and particulate organic carbon in hydrothermal plumes from the East Pacific Rise, 9150. Deep Sea Res. I 58, 922–931. doi:10.1016/j.dsr.2011.06.010

Bennett, S. a., Achterberg, E.P., Connelly, D.P., Statham, P.J., Fones, G.R., German, C.R., 2008. The distribution and stabilisation of dissolved Fe in deep-sea hydrothermal plumes. Earth Planet. Sci. Lett. 270, 157–167. doi:10.1016/j.epsl.2008.01.048

Boiteau, R.M., Mende, D.R., Hawco, N.J., McIlvin, M.R., Fitzsimmons, J.N., Saito, M.A., Sedwick, P.N., DeLong, E.F., Repeta, D.J., 2016. Siderophore-based microbial adaptations to iron scarcity across the eastern Pacific Ocean. Proc. Natl. Acad. Sci. 113, 14237–14242. doi:10.1073/pnas.1608594113

Boström, K., Peterson, M.N.A., Joensuu, O., Fisher, D.E., 1969. Aluminum-poor ferromanganoan sediments on active oceanic ridges. J. Geophys. Res. 74, 3261–3270. doi:10.1029/JB074i012p03261

Brandes, J.A., Lee, C., Wakeham, S., Peterson, M., Jacobsen, C., Wirick, S., Cody, G., 2004. Examining marine particulate organic matter at sub-micron scales using scanning transmission X-ray microscopy and carbon X-ray absorption near edge structure spectroscopy. Mar. Chem. 92, 107–121. doi:10.1016/j.marchem.2004.06.020

Brandes, J.A., Wirick, S., Jacobsen, C., 2010. Carbon K-edge spectra of carbonate minerals. J. Synchrotron Radiat. 17, 676–682. doi:10.1107/S0909049510020029

Breier, J. a., Rauch, C.G., McCartney, K., Toner, B.M., Fakra, S.C., White, S.N., German, C.R., 2009. A suspended-particle rosette multi-sampler for discrete biogeochemical sampling in

low-particle-density waters. Deep. Res. Part I Oceanogr. Res. Pap. 56, 1579–1589. doi:10.1016/j.dsr.2009.04.005

Breier, J. a., Toner, B.M., Fakra, S.C., Marcus, M. a., White, S.N., Thurnherr, a. M., German, C.R., 2012. Sulfur, sulfides, oxides and organic matter aggregated in submarine hydrothermal plumes at 9°50′N East Pacific Rise. Geochim. Cosmochim. Acta 88, 216–236. doi:10.1016/j.gca.2012.04.003

Brown, G.E., Henrich, V.E., Casey, W.H., Clark, D.L., Eggleston, C., Felmy, A., Goodman, D.W., Grtzel, M., Maciel, G., Mccarthy, M.I., Nealson, K.H., Sverjensky, D.A., Toney, M.F., Zachara, J.M., 1999. Metal Oxide Surfaces and Their Interactions with Aqueous Solutions and Microbial Organisms Microbial Organisms. Chem. Rev. 99, 77–174. doi:10.1021/cr980011z

Butler, A., 2005. Marine siderophores and microbial iron mobilization. Biometals 18, 369–374. doi:10.1007/s10534-005-3711-0

Campbell, A.C., Gieskes, J.M., Lupton, J.E., Lonsdale, P.F., 1988. Manganese gechemisty in the Guaymas Basin , Gulf of California. Methods 52, 345–357.

Chan, C.S., Fakra, S.C., Emerson, D., Fleming, E.J., Edwards, K.J., 2011. Lithotrophic iron-oxidizing bacteria produce organic stalks to control mineral growth: implications for biosignature formation. ISME J. 5, 717–727. doi:10.1038/ismej.2010.173

Charlou, L., Jean-baptiste, P., Stievenard, M., 1996. Mineral and gas chemistry of hydrothermal fluids of an ultra fast spreading ridge : East Pacific Rise , 17 ø to 19øS (Naudur cruise , 1993) phase separation processes controlled by volcanic and tectonic activity members show large variations between the. J. Geophys. Res. 101, 15,899-15,919.

Chen, C., Dynes, J.J., Wang, J., Karunakaran, C., Sparks, D.L., 2014. Soft X-ray spectromicroscopy study of mineral-organic matter associations in pasture soil clay fractions. Environ. Sci. Technol. 48, 6678–6686. doi:10.1021/es405485a

Cornell, R.M., Schwertmann, U., 2003. The iron oxides: structure, properties, reactions, occurrences and uses. John Wiley and Sons, Darmstadt, Germany.

Cowen, J.P., Bruland, K.W., 1985. Metal deposits associated with bacteria: implications for Fe and Mn marine biogeochemistry. Deep Sea Res. Part A. Oceanogr. Res. Pap. 32, 253–272. doi:10.1016/0198-0149(85)90078-0

Cowen, J.P., Massoth, G.J., Baker, E.T., 1986. Bacterial scavenging of Mn and Fe in a mid- to

872 far-field hydrothermal particle plume. Nature 322, 169–171. doi:10.1038/322169a0
873 de Vargas, C., Aubrey, M.P., Probert, I., Young, J., 2007. Origin and Evolution of
874 Coccolithophores, in: Falkowski, P.G., Knoll, A.H. (Eds.), . Elsevier, Boston, pp. 251–285.
875 Dick, G.J., Anantharaman, K., Baker, B.J., Li, M., Reed, D.C., Sheik, C.S., 2013. The
876 microbiology of deep-sea hydrothermal vent plumes: Ecological and biogeographic
877 linkages to seafloor and water column habitats. Front. Microbiol. 4, 1–16.
878 doi:10.3389/fmicb.2013.00124
879 Dick, G.J., Clement, B.G., Webb, S.M., Fodrie, F.J., Bargar, J.R., Tebo, B.M., 2009. Enzymatic
880 microbial Mn(II) oxidation and Mn biooxide production in the Guaymas Basin deep-sea
881 hydrothermal plume. Geochim. Cosmochim. Acta 73, 6517–6530.
882 doi:10.1016/j.gca.2009.07.039
883 Dick, G.J., Lee, Y.E., Tebo, B.M., 2006. Manganese(II)-Oxidizing Bacillus Spores in Guaymas
884 Basin Hydrothermal Sediments and Plumes. Appl. Environ. Microbiol. 72, 3184–3190.
885 doi:10.1128/AEM.72.5.3184–3190.2006
886 Dick, G.J., Tebo, B.M., 2010. Microbial diversity and biogeochemistry of the Guaymas Basin
887 deep-sea hydrothermal plume. Environ. Microbiol. 12, 1334–1347. doi:10.1111/j.1462-
888 2920.2010.02177.x
889 Durham, B.P., Sharma, S., Luo, H., Smith, C.B., Amin, S.A., Bender, S.J., Dearth, S.P., Van
890 Mooy, B.A.S., Campagna, S.R., Kujawinski, E.B., Armbrust, E.V., Moran, M.A., 2015.
891 Cryptic carbon and sulfur cycling between surface ocean plankton. Proc. Natl. Acad. Sci.
892 112, 453–457. doi:10.1073/pnas.1413137112
893 Dymond, J., Roth, S., 1988. Plume dispersed hydrothermal particles: A time-series record of
894 settling flux from the Endeavour Ridge using moored sensors. Geochim. Cosmochim. Acta
895 52, 2525–2536. doi:10.1016/0016-7037(88)90310-9
896 Emerson, D., 2000. Microbial oxidation of Fe(II) and Mn(II) at circumneutral pH., in:
897 Environmental Microbe-Metal Interactions. ASM Press, Washington D. C., pp. 31–52.
898 Emerson, D., Fleming, E.J., McBeth, J.M., 2010. Iron-oxidizing bacteria: an environmental and
899 genomic perspective. Annu. Rev. Microbiol. 64, 561–83.
900 doi:10.1146/annurev.micro.112408.134208
901 Feely, R.A., Lewison, M., Massoth, G.J., Robert-Baldo, G., Lavelle, J.W., Byrne, R.H., Von
902 Damm, K.L., Curl, H.C., 1987. Composition and dissolution of black smoker particulates

903 from active vents on the Juan de Fuca Ridge. J. Geophys. Res. Solid Earth 92, 11347–
904 11363. doi:10.1029/JB092iB11p11347
905 Feely, R.A., Massoth, G.J., Baker, E.T., Cowen, J.P., Lamb, M.F., Krogslund, K.A., 1990. The
906 effect of hydrothermal processes on midwater phosphorus distributions in the northeast
907 Pacific. Earth Planet. Sci. Lett. 96, 305–318. doi:10.1016/0012-821X(90)90009-M
908 Feely, R. a., Baker, E.T., Marumo, K., Urabe, T., Ishibashi, J., Gendron, J., Lebon, G.T.,
909 Okamura, K., 1996. Hydrothermal plume particles and dissolved phosphate over the
910 superfast-spreading southern East Pacific Rise. Geochim. Cosmochim. Acta 60, 2297–2323.
911 doi:10.1016/0016-7037(96)00099-3
912 Fenter, P.A., Rivers, M.L., Sturchio, N.C., Sutton, S.R., 2002. Reviews in Mineralogy and
913 Geochemistry Volume 49: Applications of Synchrotron Radiation in Low-Temperature
914 Geochemistry and Environmental Science. Geochemical Society, Chicago, Illinois, USA.
915 doi:https://doi.org/10.2138/gsrmg.49.1.vii
916 Field, M.P., Sherrell, R.M., 2000. Dissolved and particulate Fe in a hydrothermal plume at
917 9°45′N, East Pacific Rise: Geochim. Cosmochim. Acta 64, 619–628. doi:10.1016/S0016-
918 7037(99)00333-6
919 Fisher, C., Takai, K., Le Bris, N., 2007. Hydrothermal Vent Ecosystems. Oceanography 20, 14–
920 23. doi:10.5670/oceanog.2007.75
921 Fitzsimmons, J.N., Boyle, E. a., Jenkins, W.J., 2014. Distal transport of dissolved hydrothermal
922 iron in the deep South Pacific Ocean. Proc. Natl. Acad. Sci. 111, 16654–16661.
923 doi:10.1073/pnas.1418778111
924 Fitzsimmons, J.N., John, S.G., Marsay, C.M., Hoffman, C.L., Nicholas, S.L., Toner, B.M.,
925 German, C.R., Sherrell, R.M., 2017. Iron persistence in a distal hydrothermal plume
926 supported by dissolved-particulate exchange. Nat. Geosci. 10. doi:10.1038/ngeo2900
927 German, C., Seyfried, W.E., 2014. Hydrothermal Processes, 2nd ed, Elsevier. Elsevier Ltd.
928 doi:10.1016/B978-0-08-095975-7.00201-1
929 German, C.R., Legendre, L.L., Sander, S.G., Niquil, N., Luther, G.W., Bharati, L., Han, X., Le
930 Bris, N., 2015. Hydrothermal Fe cycling and deep ocean organic carbon scavenging:
931 Model-based evidence for significant POC supply to seafloor sediments. Earth Planet. Sci.
932 Lett. 419, 143–153. doi:10.1016/j.epsl.2015.03.012
933 Gillespie, A.W., Phillips, C.L., Dynes, J.J., Chevrier, D., Regier, T.Z., Peak, D., 2015. Advances

in Using Soft X-Ray Spectroscopy for Measurement of Soil Biogeochemical Processes, Advances in Agronomy. Elsevier Ltd. doi:10.1016/bs.agron.2015.05.003

Gillespie, A.W., Sanei, H., Diochon, A., Ellert, B.H., Regier, T.Z., Chevrier, D., Dynes, J.J., Tarnocai, C., Gregorich, E.G., 2014. Perennially and annually frozen soil carbon differ in their susceptibility to decomposition: Analysis of Subarctic earth hummocks by bioassay, XANES and pyrolysis. Soil Biol. Biochem. 68, 106–116. doi:10.1016/j.soilbio.2013.09.021

Golchin, A., Oades, J.M., Skjemstad, J.O., Clarke, P., 1994. Study of Free and Occluded Particulate Organic Matter in Soils by Solid state 13C CP/MAS\nNMR Spectroscopy and Scanning Electron Microscopy. Aust. J. Soil Res. 32, 285–309. doi:10.1071/SR9940285

Hawkes, J.A., Connelly, D.P., Gledhill, M., Achterberg, E.P., 2013. The stabilisation and transportation of dissolved iron from high temperature hydrothermal vent systems. Earth Planet. Sci. Lett. 375, 280–290. doi:10.1016/j.epsl.2013.05.047

Heller, M.I., Lam, P.J., Moffett, J.W., Till, C.P., Lee, J.-M., Toner, B.M., Marcus, M.A., 2017. Accumulation of Fe oxides in the Peruvian oxygen deficient zone implies non-oxygen dependent Fe oxidation. Geochim. Cosmochim. Acta Submitted. doi:10.1016/j.gca.2017.05.019

Hem, J.D., 1981. Rates of manganese oxidation in aqueous systems Wwtl. Geochim. Cosmochim. Acta 45, 1369–1374.

Hem, J.D., Lind, C.J., 1983. Nonequilibrium models for predicting forms of precipitated manganese oxides. Geochim. Cosmochim. Acta 47, 2037–2046. doi:10.1016/0016-7037(83)90219-3

Hitchcock, A.P., 2016. aXis 2000- Analysis of X-ray Images and Spectra [WWW Document]. URL http://unicorn.mcmaster.ca/aXis2000.html

Holden, J., Breier, J., Rogers, K., Schulte, M., Toner, B., 2012. Biogeochemical processes at hydrothermal vents: microbes and minerals, bioenergetics, and carbon fluxes. Oceanography 25, 196–208. doi:http://dx.doi.org/10.5670/oceanog.2012.18

Hsu-Kim, H., Mullaugh, K.M., Tsang, J.J., Yucel, M., Luther, G.W., 2008. Formation of Zn- and Fe-sulfides near hydrothermal vents at the Eastern Lau Spreading Center: implications for sulfide bioavailability to chemoautotrophs. Geochem. Trans. 9, 6. doi:10.1186/1467-4866-9-6

Jenkins, W.J., Lott, D.E., German, C.R., Cahill, K.L., Goudreau, J., Longworth, B., 2017. The

965 deep distributions of helium isotopes, radiocarbon, and noble gases along the U.S.
966 GEOTRACES East Pacific Zonal Transect (GP16). Mar. Chem. 0–1.
967 doi:10.1016/j.marchem.2017.03.009
968 Jiang, H., Breier, J.A., 2014. Physical controls on mixing and transport within rising submarine
969 hydrothermal plumes: A numerical simulation study. Deep. Res. Part I Oceanogr. Res. Pap.
970 92, 41–55. doi:10.1016/j.dsr.2014.06.006
971 Johnson, J.E., Savalia, P., Davis, R., Kocar, B.D., Webb, S.M., Nealson, K.H., Fischer, W.W.,
972 2016. Real-Time Manganese Phase Dynamics during Biological and Abiotic Manganese
973 Oxide Reduction. Environ. Sci. Technol. 50, 4248–4258. doi:10.1021/acs.est.5b04834
974 Kadar, E., Fisher, A., Stolpe, B., Harrison, R.M., Parello, F., Lead, J., 2012. Metallic
975 nanoparticle enrichment at low temperature, shallow CO 2 seeps in Southern Italy. Mar.
976 Chem. 140–141, 24–32. doi:10.1016/j.marchem.2012.07.001
977 Kadko, D.C., Rosenberg, N.D., Lupton, J.E., Collier, R.W., Lilley, M.D., 1990. Chemical
978 reaction rates and entrainment within the Endeavor Ridge hydrothermal plume. Earth
979 Planet. Sci. Lett. 99, 315–335.
980 Keil, R.G., Tsamakis, E., Bor Fuh, C., Giddings, J.C., Hedges, J.I., 1993. Mineralogic controls
981 on the concentration and elemental composition of organic-matter in marine sediments:
982 Hydrodynamic separation using Splitt-fractionation 58, 879–893.
983 Kessick, M.A., Morgan, J.J., 1975. Mechanism of autooxidation of manganese in aqueous
984 solution. Environ. Sci. Technol. 9, 157–159.
985 Kilcoyne, a L.D., Tyliszczak, T., Steele, W.F., Fakra, S., Hitchcock, P., Franck, K., Anderson,
986 E., Harteneck, B., Rightor, E.G., Mitchell, G.E., Hitchcock, a P., Yang, L., Warwick, T.,
987 Ade, H., 2003. Interferometer-controlled scanning transmission X-ray microscopes at the
988 Advanced Light Source. J. Synchrotron Radiat. 10, 125–36.
989 Kipp, L.E., Sanial, V., Henderson, P.B., van Beek, P., Reyss, J.L., Hammond, D.E., Moore,
990 W.S., Charette, M.A., n.d. Radium isotopes as tracers of hydrothermal inputs and neutrally
991 buoyant plume dynamics in the deep ocean. Mar. Chem.
992 Kostka, J., Luther III, G.W., Nealson, K.H., 1995. Chemical and biological reduction of Mn(III)-
993 pyrophosphate complexes: Potential importance of dissolved Mn(III) as an environmental
994 oxidant. Geochim. Cosmochim. Acta 59, 885–894. doi:10.1016/00167-0379(50)00070-
995 Kraft, S., Stümpel, J., Becker, P., Kuetgens, U., 1996. High resolution x-ray absorption

spectroscopy with absolute energy Calibration for the determination of absorption edge energies. Rev. Sci. Instrum. 67, 681–687. doi:10.1063/1.1146657

Ksionzek, K.B., Schmitt-Kopplin, P., Koch, B.P., 2016. Dissolved organic sulfur in the ocean-Biogeochemistry of a petagram inventory. Science (80-.). 354, 456–459.

Lam, P.J., Lee, J.-M., Heller, M.I., Mehic, S., Xiang, Y., Bates, N.R., 2017. Size-fractionated distributions of suspended particle concentration and major phase composition from the U.S. GEOTRACES Eastern Pacific Zonal Transect (GP16). Mar. Chem. In review, 0–1. doi:10.1016/

Lam, P.J., Ohnemus, D.C., Marcus, M. a., 2012. The speciation of marine particulate iron adjacent to active and passive continental margins. Geochim. Cosmochim. Acta 80, 108–124. doi:10.1016/j.gca.2011.11.044

Lee, J.-M., Heller, M.I., Lam, P.J., 2017. Size distribution of particulate trace elements in the U.S. GEOTRACES Eastern Pacific Zonal Transect (GP16). Mar. Chem. In press, 0–1. doi:10.1016/j.marchem.2017.09.006

Lewis, B.L., Holt, P.D., Taylor, S.W., Wilhelm, S.W., Trick, C.G., Butler, A., Luther III, G.W., Others, 1995. Voltammetric estimation of iron (III) thermodynamic stability constants for catecholate siderophores isolated from marine bacteria and cyanobacteria. Mar. Chem. 50, 179–188.

Li, M., Toner, B.M., Baker, B.J., Breier, J. a, Sheik, C.S., Dick, G.J., 2014. Microbial iron uptake as a mechanism for dispersing iron from deep-sea hydrothermal vents. Nat. Commun. 5, 3192. doi:10.1038/ncomms4192

Lilley, M.D., Feely, R.A., Trefry, J.H., 1995. Chemical and Biochemical Transformations in Hydrothermal Plumes, in: Humphris, S.E., Zierenberg, R.A., Mullineaux, L.S., Thomson, R.E. (Eds.), Seafloor Hydrothermal Systems: Physical, Chemical, Biological, and Geological Interactions (. American Geophysical Union, Washington D. C. doi:10.1029/GM091p0369

Luther, G.W., Rozan, T.F., Taillefert, M., Nuzzio, D.B., Di Meo, C., Shank, T.M., Lutz, R. a, Cary, S.C., 2001. Chemical speciation drives hydrothermal vent ecology. Nature 410, 813–816. doi:10.1038/35071069

Lyle, M.W., 1986. Major element composition of leg-92 sediments. Initial Reports of the Deep Sea Drilling Project 92.

Mandernack, K.W., Tebo, B.M., 1993. Manganese scavenging and oxidation at hydrothermal vents and in vent plumes. Geochim. Cosmochim. Acta 57, 3907–3923. doi:10.1016/0016-7037(93)90343-U

Marcus, M.A., Westphal, A.J., Fakra, S.C., 2008. Classification of Fe-bearing species from K-edge XANES data using two-parameter correlation plots. J. Synchrotron Radiat. 15, 463–468. doi:10.1107/S0909049508018293

Marcus, M. a, MacDowell, A. a, Celestre, R., Manceau, A., Miller, T., Padmore, H. a, Sublett, R.E., 2004. Beamline 10.3.2 at ALS: a hard X-ray microprobe for environmental and materials sciences. J. Synchrotron Radiat. 11, 239–47. doi:10.1107/S0909049504005837

Navrotsky, A., Mazeina, L., Majzlan, J., 2008. Size-driven structural and thermodynamic complexity in iron oxides. Science 319, 1635–8. doi:10.1126/science.1148614

Nealson, K.H., Rosson, R.A., Myers, C.R., 1989. Mechanisms of oxidation and reduction of manganese, in: Metal Ions and Bacteria. John Wiley and Sons, New York.

Nicholas, S.L., Erickson, M.L., Woodruff, L.G., Knaeble, A.R., Marcus, M.A., Lynch, J.K., Toner, B.M., 2017. Solid-phase arsenic speciation in aquifer sediments: A micro-X-ray absorption spectroscopy approach for quantifying trace-level speciation. Geochim. Cosmochim. Acta 211, 228–255. doi:10.1016/j.gca.2017.05.018

Nishioka, J., Obata, H., Tsumune, D., 2013. Evidence of an extensive spread of hydrothermal dissolved iron in the Indian Ocean. Earth Planet. Sci. Lett. 361, 26–33. doi:10.1016/j.epsl.2012.11.040

O'day, P.A., Rivera Jr., N., Root, R., Carroll, S.A., 2004. X－ray absorption spectroscopic study of Fe reference compouds for the analysis of natural sediments.pdf. Am. Mineral. 89, 572–585.

Ohnemus, D.C., Lam, P.J., 2015. Cycling of lithogenic marine particles in the US GEOTRACES North Atlantic transect. Deep. Res. Part II Top. Stud. Oceanogr. 116, 283–302. doi:10.1016/j.dsr2.2014.11.019

Ohnemus, D.C., Rauschenberg, S., Cutter, G.A., Fitzsimmons, J.N., Sherrell, R.M., Twining, B.S., 2016. Elevated trace metal content of prokaryotic communities associated with marine oxygen deficient zones. Limnol. Oceanogr. 62, 3–25. doi:10.1002/lno.10363

Olins, H.C., Rogers, D.R., Preston, C., Iii, W.U., 2017. Co-registered Geochemistry and Metatranscriptomics Reveal Unexpected Distributions of Microbial Activity within a

Hydrothermal Vent Field. Front. Microbiol. 8, 1–18. doi:10.3389/fmicb.2017.01042

Post, J.E., 1999. Manganese oxide minerals : Crystal structures and economic and. Proc. Natl. Acad. Sci. 96, 3447–3454.

Ravel, B., Newville, M., 2005. ATHENA, ARTEMIS, HEPHAESTUS: Data analysis for X-ray absorption spectroscopy using IFEFFIT. J. Synchrotron Radiat. 12, 537–541. doi:10.1107/S0909049505012719

Reed, D.C., Breier, J. a, Jiang, H., Anantharaman, K., Klausmeier, C. a, Toner, B.M., Hancock, C., Speer, K., Thurnherr, A.M., Dick, G.J., 2015. Predicting the response of the deep-ocean microbiome to geochemical perturbations by hydrothermal vents. ISME J. 1–13. doi:10.1038/ismej.2015.4

Resing, J. a., Sedwick, P.N., German, C.R., Jenkins, W.J., Moffett, J.W., Sohst, B.M., Tagliabue, A., 2015. Basin-scale transport of hydrothermal dissolved metals across the South Pacific Ocean. Nature 523, 200–203. doi:10.1038/nature14577

Rue, E.L., Bruland, K.W., 1995. Complexation of iron(lll) by natural organic ligands in the Central North Pacific as determined by a new competitive ligand equilibration/adsorptive cathodic stripping voltammetric method. Mar. Chem. 50, 117–138. doi:10.1016/0304-4203(95)00031-L

Saito, M.A., Noble, A.E., Tagliabue, A., Goepfert, T.J., Lamborg, C.H., Jenkins, W.J., 2013. Slow-spreading submarine ridges in the South Atlantic as a significant oceanic iron source. Nat. Geosci. 6, 775–779. doi:10.1038/ngeo1893

Sander, S.G., Koschinsky, A., 2011. Metal flux from hydrothermal vents increased by organic complexation. Nat. Geosci. 4, 145–150. doi:10.1038/ngeo1088

Sander, S.G., Koschinsky, A., Massoth, G., Stott, M., Hunter, K.A., 2007. Organic complexation of copper in deep-sea hydrothermal vent systems. Environ. Chem. 4, 81–89. doi:10.1071/EN06086

Sands, C.M., Connelly, D.P., Statham, P.J., German, C.R., 2012. Size fractionation of trace metals in the Edmond hydrothermal plume, Central Indian Ocean. Earth Planet. Sci. Lett. 319–320, 15–22. doi:10.1016/j.epsl.2011.12.031

Santelli, C.M., Webb, S.M., Dohnalkova, A.C., Hansel, C.M., 2011. Diversity of Mn oxides produced by Mn(II)-oxidizing fungi. Geochim. Cosmochim. Acta 75, 2762–2776. doi:10.1016/j.gca.2011.02.022

1089 Sayles, F.L., Martin, W.R., Chase, Z., Anderson, R.F., 2001. Benthic remineralization and burial
1090 of biogenic SiO2, CaCO3, organic carbon, and detrital material in the Southern Ocean along
1091 a transect at 170° West. Deep. Res. Part II Top. Stud. Oceanogr. 48, 4323–4383.
1092 doi:10.1016/S0967-0645(01)00091-1
1093 Sedlmair, J., Gleber, S.C., Peth, C., Mann, K., Niemeyer, J., Thieme, J., 2012. Characterization
1094 of refractory organic substances by NEXAFS using a compact X-ray source. J. Soils
1095 Sediments 12, 24–34. doi:10.1007/s11368-011-0385-9
1096 Sheik, C.S., Anantharaman, K., Breier, J.A., Sylvan, J.B., Edwards, K.J., Dick, G.J., 2015.
1097 Spatially resolved sampling reveals dynamic microbial communities in rising hydrothermal
1098 plumes across a back-arc basin. ISME J. 9, 1434–45. doi:10.1038/ismej.2014.228
1099 Shimmield, B., Price, N.B., 1988. The scavenging of U, 230Th and 231Pa during pulsed
1100 hydrothermal activity at 20S, East Pacific Rise. Geochim. Cosmochim. Acta 52, 669–677.
1101 doi:10.1016/0016-7037(88)90329-8
1102 Stöhr, J., 2003. NEXAFS Spectroscopy, Second. ed. Springer, Heidelberg, Germany.
1103 Tebo, B.M., Bargar, J.R., Clement, B.G., Dick, G.J., Murray, K.J., Parker, D., Verity, R., Webb,
1104 S.M., 2004. BIOGENIC MANGANESE OXIDES: Properties and Mechanisms of
1105 Formation. Annu. Rev. Earth Planet. Sci. 32, 287–328.
1106 doi:10.1146/annurev.earth.32.101802.120213
1107 Tivey, M., 2007. Generation of Seafloor Hydrothermal Vent Fluids and Associated Mineral
1108 Deposits. Oceanography 20, 50–65. doi:10.5670/oceanog.2007.80
1109 Tivey, M.K., McDuff, R.E., 1990. Mineral precipitation in the walls of black smoker chimneys:
1110 A quantitative model of transport and chemical reaction. J. Geophys. Res. 95, 12617.
1111 doi:10.1029/JB095iB08p12617
1112 Toner, B., Fakra, S., Villalobos, M., Warwick, T., Sposito, G., 2005. Spatially Resolved
1113 Characterization of Biogenic Manganese Oxide Production within a Bacterial Biofilm.
1114 Appl. Environ. Microbiol. 71, 1300–1310. doi:10.1128/AEM.71.3.1300
1115 Toner, B., Marcus, M., Edwards, K., Rouxel, O., German, C.R., 2012. Measuring the form of
1116 iron in hydrothermal plume particles. Oceanography 25, 209–212.
1117 doi:http://dx.doi.org/10.5670/oceanog.2012.19
1118 Toner, B.M., Fakra, S.C., Manganini, S.J., Santelli, C.M., Marcus, M. a., Moffett, J.W., Rouxel,
1119 O., German, C.R., Edwards, K.J., 2009a. Preservation of iron(II) by carbon-rich matrices in

a hydrothermal plume. Nat. Geosci. 2, 197–201. doi:10.1038/ngeo433

Toner, B.M., German, C.R., Dick, G.J., Breier, J.A., 2016. Deciphering the Complex Chemistry of Deep-Ocean Particles Using Complementary Synchrotron X-ray Microscope and Microprobe Instruments. Acc. Chem. Res. 49, 128–137. doi:10.1021/acs.accounts.5b00282

Toner, B.M., Nicholas, S.L., Coleman Wasik, J.K., 2014. Scaling up : fulfilling the promise of X-ray microprobe for biogeochemical research. Environ. Chem. doi:http://dx.doi.org/10.1071/EN13162

Toner, B.M., Santelli, C.M., Marcus, M. a., Wirth, R., Chan, C.S., McCollom, T., Bach, W., Edwards, K.J., 2009b. Biogenic iron oxyhydroxide formation at mid-ocean ridge hydrothermal vents: Juan de Fuca Ridge. Geochim. Cosmochim. Acta 73, 388–403. doi:10.1016/j.gca.2008.09.035

Trouwborst, R.E., Clement, B.G., Tebo, B.M., Glazer, B.T., Iii, G.W.L., 2006. Soluble Mn (III) in suboxic zones. Science (80-.). 1955, 1955–1957. doi:10.1126/science.1132876

Urquhart, S.G., Ade, H., 2002. Trends in the Carbonyl Core (C 1s, O 1s) ®p*C=O Transition in the Near Edge X-ray Absorption Fine Structure Spectra of Organic Molecules. J. Phys. Chem. B 106, 8531–8538.

Van Dover, C.L., 2000. The ecology of deep-sea hydrothermal vents. Princeton University Press, Princeton, NJ.

Villalobos, M., Toner, B., Bargar, J., Sposito, G., 2003. Characterization of the manganese oxide produced by Pseudomonas putida strain MnB1. Geochim. Cosmochim. Acta 67, 2649–2662. doi:10.1016/S0016-7037(03)00217-5

von der Heyden, B.P., Roychoudhury, A.N., Mtshali, T.N., Tyliszczak, T., Myneni, S.C.B., 2012. Chemically and Geographically Distinct Solid-Phase Iron Pools in the Southern Ocean. Science (80-.). 338, 1199–1201. doi:10.2960/J.v42.m652

Webb, S.M., 2005. SIXPack a Graphical User Interface for XAS Analysis Using IFEFFIT. Phys. Scr. T115, 1011–1014. doi:10.1238/Physica.Topical.115a01011

Webb, S.M., Dick, G.J., Bargar, J.R., Tebo, B.M., 2005. Evidence for the presence of Mn(III) intermediates in the bacterial oxidation of Mn(II). Proc. Natl. Acad. Sci. U. S. A. 102, 5558–63. doi:10.1073/pnas.0409119102

Weishaar, J.L., Aiken, G.R., Bergamaschi, B.A., Fram, M.S., Fujii, R., Mopper, K., 2003. Evaluation of specific ultraviolet absorbance as an indicator of the chemical composition

and reactivity of dissolved organic carbon. Environ. Sci. Technol. 37, 4702–4708. doi:10.1021/es030360x

Welter, E., Calmano, W., Mangold, S., Tröger, L., 1999. Chemical speciation of heavy metals in soils by use of XAFS spectroscopy and electron microscopical techniques. Fresenius. J. Anal. Chem. 364, 238–244. doi:10.1007/s002160051330

Wu, J., Luther, G.W., 1995. Complexation of Fe (III) by natural organic ligands in the Northwest Atlantic Ocean by a competitive ligand equilibration method and a kinetic approach. Mar. Chem. 50, 159–177.

Wu, J., Wells, M.L., Rember, R., 2011. Dissolved iron anomaly in the deep tropical-subtropical Pacific: Evidence for long-range transport of hydrothermal iron. Geochim. Cosmochim. Acta 75, 460–468. doi:10.1016/j.gca.2010.10.024

Yücel, M., Gartman, A., Chan, C.S., Luther, G.W., 2011. Hydrothermal vents as a kinetically stable source of iron-sulphide-bearing nanoparticles to the ocean. Nat. Geosci. 4, 367–371. doi:10.1038/ngeo1148

Zeng, T., Arnold, W.A., Toner, B.M., 2013. Microscale characterization of sulfur speciation in lake sediments. Environ. Sci. Technol. 47, 1287–1296. doi:10.1021/es303914q

Ziervogel, K., Forster, S., 2005. Aggregation and sinking behaviour of resuspended fluffy layer material. Cont. Shelf Res. 25, 1853–1863. doi:10.1016/j.csr.2005.06.008

Figure Captions

Figure 1. Bulk Chemistry Profiles

Depth distribution of total particulate organic carbon (POC_tot), total particulate inorganic carbon (TIC_tot), total particulate Fe (pFe_tot), and total particulate Mn (pMn_tot) for Station 17 (up-current from the ridge axis), Station 18 (over ridge axis), and Station 20 (83 km down-current from the ridge axis).

Figure 2: Bulk XANES of Station 20 fluff layer.

(a) Carbon 1s XANES spectrum plotted with three calcite reference spectra having different crystal orientations (Brandes et al., 2010). (b) Iron 1s XANES spectrum plotted with three Fe(III) oxyhydroxide standards (Toner et al., 2009b). (c) Manganese 1s XANES spectrum plotted with three Mn oxide standards (Bargar et al., 2000; Villalobos et al., 2003). Identifying features and peaks are highlighted.

Figure 3: Station 18 STXM elemental maps and C 1s XANES

Transmission images were collected at 290 eV (a,d, g). Total carbon optical density ranges from 1.12 (b), 1.35 (e), and 0.994 (h). Total iron optical density ranges from 0.0595 (c), 2.83 (f), and 0.584 (i). Scale bars for a-b 500nm, c is 200 nm, d-f are 5µm, and g-i are 1µm. Carbon 1s XANES spectra from the above plume background, plume middle, and plume bottom are compared to standards protein (BSA), phosphatidylethanolamine (PE) lipid, and lipid (j) (Chan et al., 2011). The green bar highlights the ~285 eV peak corresponding to the 1s-$\pi^*_{C=C}$ transition. The blue bar highlights the unique signatures of organic carbon.

Figure 4: Station 20 STXM elemental maps and C 1s XANES

Transmission images were collected at 290 eV (a, d, g, j, and m). Total carbon optical density ranges from 1.10 (b), 1.50 (e), 0.0.853 (h), 1.36 (k), and 0.927 (n). Total iron optical density ranges from 1.69 (c), 2.57 (f), 2.85 (i), 0.961 (l), and 2.61 (o). Scale bars for (a-i, m, and n) are 5µm, (j-l) are 2µm, and (o) is 10µm. Carbon 1s XANES spectra from the plume top, plume middle, plume bottom, near bottom background, and benthic fluff layer are compared to standards protein (BSA), PE lipid, lipid, and calcite (p) (Brandes et al., 2010; Chan et al., 2011).

The green bar highlights the ~285 eV peak corresponding to the 1s-$\pi^*_{C=C}$ transition. The blue bar highlights the unique signatures of organic carbon, while the yellow bar corresponds to distinct peaks associated with inorganic carbon. With the benthic fluff layer data we are able to identify both organic and inorganic signatures.

Figure 5: Near-field Fe 2p XANES

Iron 2p XANES spectra from the plume middle and plume bottom at Station 18 (a) and Station 20 (b) are compared to standards pyrite, siderite, ferrihydrite and goethite. Peaks from both Station 18 and 20 are most similar with those of ferrihydrite (Toner et al., 2009a). Identifying features and peaks are highlighted**.**

Figure 6: Near-field Fe 1s µXANES

Particulate Fe speciation profiles for Station 18 and 20. All values were generated by linear least-squares fitting of point-XANES data (Fe 1s absorption edge) and post-analysis binning into broad Fe species groups. GEOTRACES numbers, water depth and other characteristics are in Table 1. A) Samples for above plume background and plume top, middle, and bottom were analyzed for Station 18. B) Samples for plume middle, near bottom background, and benthic fluff layer were analyzed for Station 20. C) Percent Fe species on per atom basis for all Station 18 and 20 samples are summarized. These values are sums of Fe species observed divided by the total number of observations; no statistical model applied. The error estimate for each species bin is less than 5 atom % (Bargar et al., 2005; Nicholas et al., 2017; O'day et al., 2004; Welter et al., 1999). See section 3.3.2 for discussion of the native Fe and sulfide components of the above plume background sample.

Supplemental Information Figure Captions

Figure S1. X-ray fluorescence (XRF) maps of total iron, total manganese, and total calcium for the above plume background and top, middle, and bottom plume samples at Station 18. All scale bars 200 micron.

Figure S2. X-ray fluorescence (XRF) maps of total iron, total manganese, and total calcium for the plume middle, near bottom background, and benthic fluff layer samples at Station 20. All scale bars 200 micron.

Figure S3: Station 18 STXM elemental maps of the above plume background

All marine particles analyzed at the above plume background (1600 m). Transmission images were collected at 290 eV (a, c, e, h, and k). Total carbon optical density ranges from 1.44 (b), 1.07 (d), 1.12 (f), 1.04 (i), and 0.990 (l). Total iron optical density ranges from 0.0595 (g), 1.86 (f), and 0.302 (i). In some case, and iron map was not run due to no iron being detected in those samples. Scale bars for a-d are 2µm, e and f are 500nm, g is 200nm, h-j are 5µm, and all others are 1µm. Carbon 1s XANES spectra from the above plume background (n).

Figure S4: Station 18 STXM elemental maps of the middle of the plume

All marine particles analyzed in the middle of the plume at Station 18 (2500 m). Transmission images were collected at 290 eV (a, d, g, j, l, o, and r). Total carbon optical density ranges from 1.35 (b), 1.59 (e), 1.01 (h), 1.87 (k), 1.25 (m), 1.82 (p), and 0.713 (s). Total iron optical density ranges from 2.83 (c), 1.67 (f), 2.27 (i), 2.26 (n), 2.91 (q), and 2.44 (t). For Zone_04 Mar14 an iron elemental map was not collected. Scale bars for a-c, o-q are 5µm, g-n are 2µm, and all others are 1µm. Carbon 1s XANES spectra from the middle of the plume at station 18 (u).

Figure S5: Station 18 STXM elemental maps of the bottom of the plume

All marine particles analyzed at the bottom of Station 18 (2610 m). Transmission images were collected at 290 eV (a, c, e, g, i, l, and o). Total carbon optical density ranges from 1.90 (b), 1.51 (d), 1.60 (f), 0.670 (h), 0.994 (j), 0.606 (m), and 0.580 (p). Total iron optical density ranges from 0.584 (k), 0.854 (n), and 0.472 (q). For particles collect in March 2014, iron elemental maps

were not collected. Scale bars a, b, j-n are 2µm, c-d, g-h are 500nm, and all others are 1µm. Carbon 1s XANES spectra from the bottom of the plume at station 18 (u).

Figure S6: Station 20 STXM elemental maps of the top of the plume

All marine particles analyzed the top of the plume at Station 20 (2350 m). Transmission images were collected at 290 eV (a, c, f, and i). Total carbon optical density ranges from 1.10 (d), 1.20 (g), and 1.28 (j). Total iron optical density ranges from 0.244 (b), 1.69 (e), and 0.411 (h). The carbon elemental map was corrupted for zone_00_A Mar14 and no iron map was collected for Zone_01_B Feb15. Scale bars for a-b are 2µm, and all others are 5µm. Carbon 1s XANES spectra from the top of the plume at station 20 (k).

Figure S7: Station 20 STXM elemental maps of the middle of the plume

All marine particles analyzed in the middle of the plume at Station 20 (2550 m). Transmission images were collected at 290 eV (a, d, g, j, m, p, and s). Total carbon optical density ranges from 1.50 (b), 1.81 (e), 1.53 (h), 1.20 (k), 0.628 (n), 0.688 (q), and 0.689 (t). Total iron optical density ranges from 2.57 (c), 2.55 (f), 2.27 (i), 1.73 (l), 3.02 (o), 2.67 (r), and 2.82 (u). Scale bars for a-c, m-u are 5µm, d-f are 2µm, g-j are 1µm, and j-l are 500nm. Zone_01 Mar14 was previously published in Fitzsimmons et al., 2017. Carbon 1s XANES spectra from the middle of the plume at station 20 (v).

Figure S8: Station 20 STXM elemental maps of the bottom of the plume

All marine particles analyzed at the bottom of the plume at station 20 (2600 m). Transmission images were collected at 290 eV (a, d, f, and i). Total carbon optical density ranges from 1.25 (b), 0.754 (g), and 0.853 (j). Total iron optical density ranges from 1.82 (c), 2.33 (e), 2.54 (h), and 2.85 (k). Scale bars for a-c are 500nm, d, i-k are 5µm, and e, f-h are 2µm. Carbon 1s XANES spectra from the bottom of the plume at station 20 (l).

Figure S9: Station 20 STXM elemental maps of the near bottom background

All marine particles analyzed at the near bottom background at Station 20 (3140 m). Transmission images were collected at 290 eV (a,d,f, and i). Total carbon optical density ranges from 1.36 (b), 0.535 (e), 1.25 (g), and 1.88 (j). Total iron optical density ranges from 0.961 (c),

1.67 (h), and 1.88 (k). An iron elemental map was not collected at zone_00_B Mar14. Scale bars for (a-c) are 2µm, (d-e) are 500nm, and all others are 1µm. Rod-shaped (d-e, g) and spherical cells (b) were commonly observed throughout this sample. Carbon 1s XANES spectra from the near bottom background (l).

Figure S10: Station 20 STXM elemental maps of the fluff layer

All marine particles analyzed by STXM at the station 20 fluff layer (3178 m). Transmission images were collected at 290 eV (a, d, and g). Total carbon optical density ranges from 2.61 (b), 2.21 (e), and 2.31 (h). Total iron optical density ranges from 0.927 (c), 1.23 (f), and 1.28 (i). The red rectangle in Zone 00 (c) refers to the area mapped in (a) and (b). The scale bar for c is 10µm. All other scale bars are 5µm. Carbon 1s XAS spectra from the fluff layer at station 20 (j).

Figure S11. Frequency distribution of Fe-bearing standards in linear combination fitting of microprobe Fe 1s XANES data.

Figure S12. X-ray fluorescence (XRF) tricolor maps for above plume background and top, middle, and bottom plume samples at Station 18. Column left (FeMnCa), center (CuNiZn), and right (FeTiCa) are shown in red, green, blue. All scale bars 200 micron.

Figure S13. X-ray fluorescence (XRF) tricolor maps for the plume middle, near bottom background, and benthic fluff layer samples at Station 20. Column left (FeMnCa), center (CuNiZn), and right (FeTiCa) are shown in red, green, blue. All scale bars 200 micron.

Fig.1

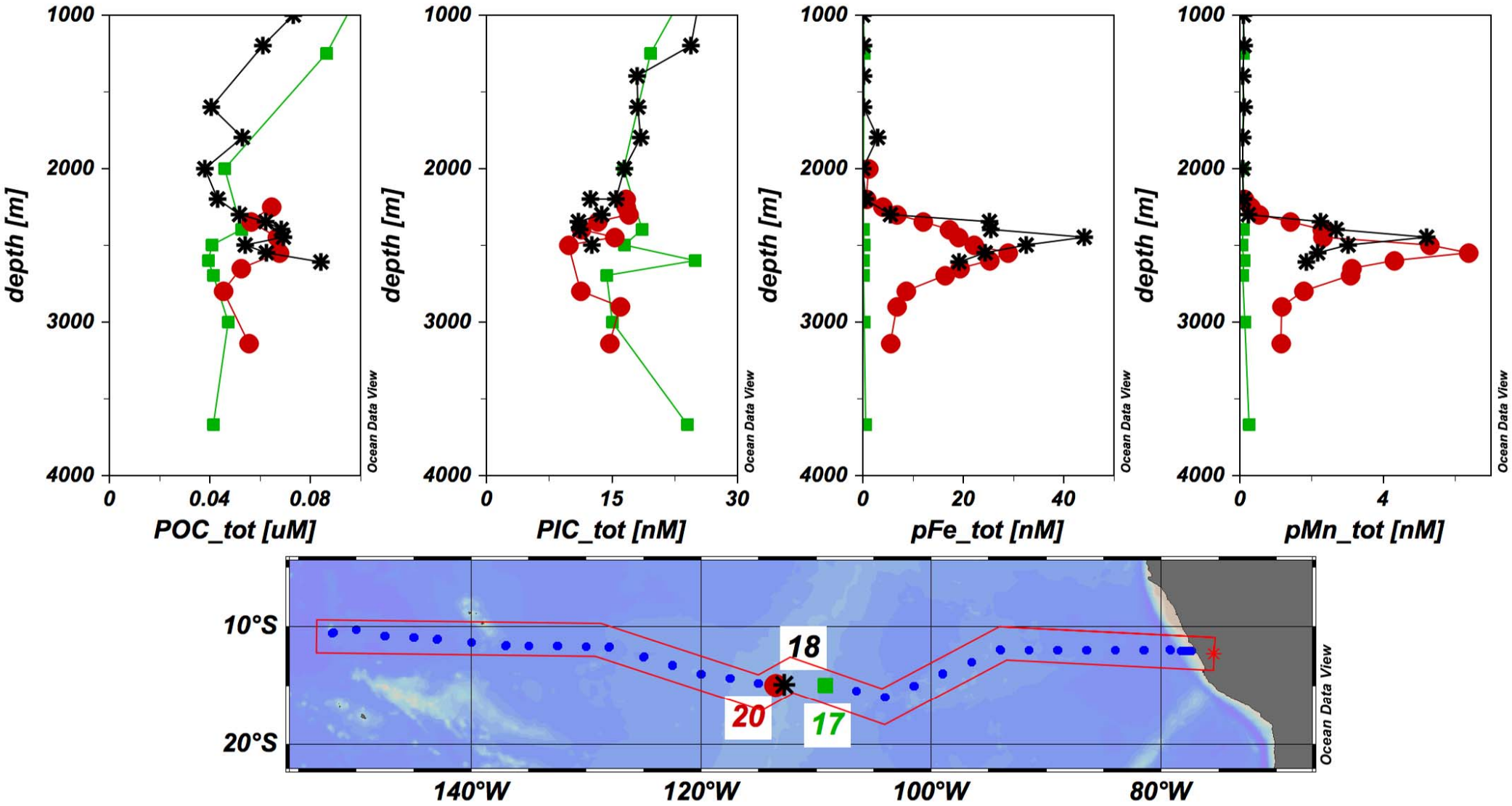
depth [m]
1000
2000
3000
4000
0
0.04
0.08
POC_tot [uM]
15
30
PIC_tot [nM]
20
40
pFe_tot [nM]
4
pMn_tot [nM]
Ocean Data View
10°S
20°S
140°W
120°W
100°W
80°W
18
20
17

Fig.2

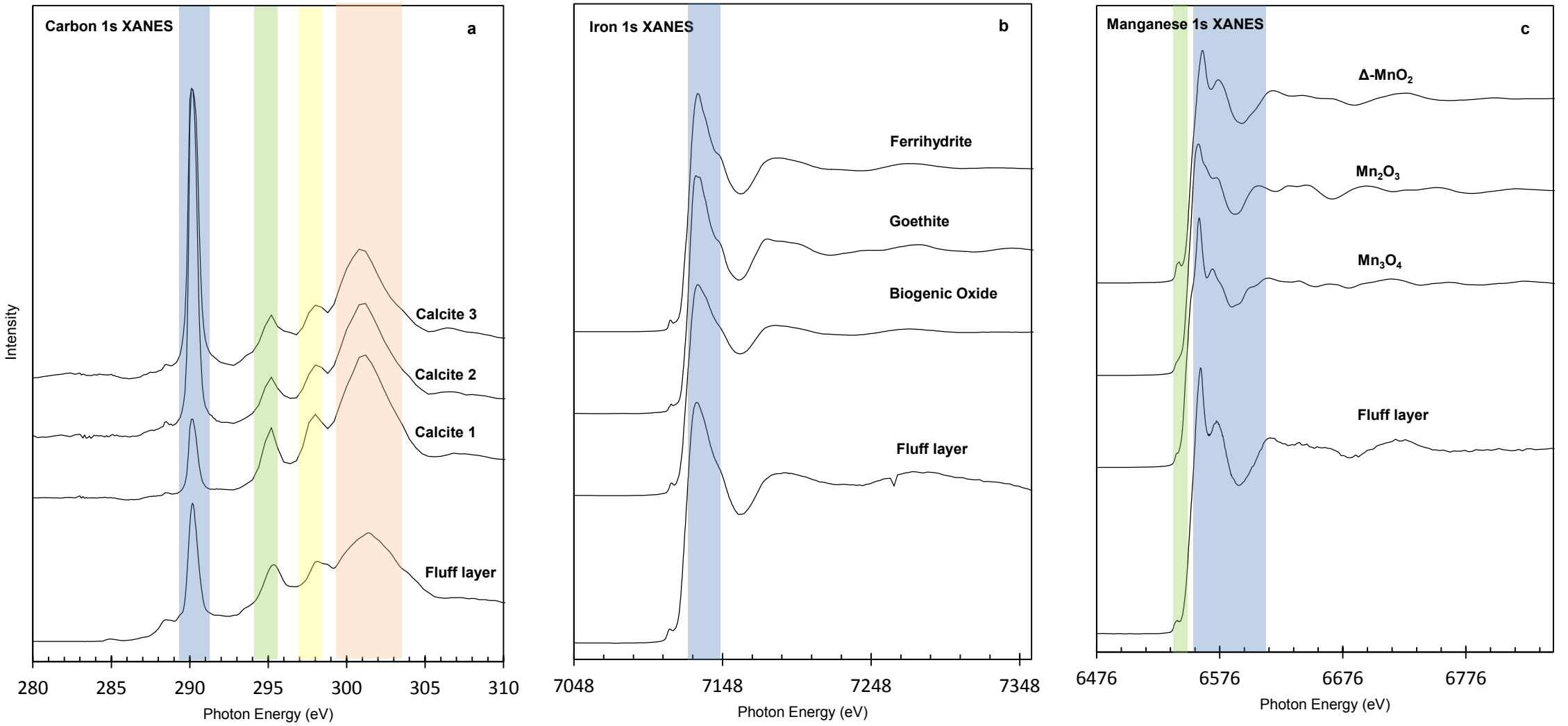
Carbon 1s XANES
a
Intensity
Calcite 3
Calcite 2
Calcite 1
Fluff layer
280
285
290
295
300
305
310
Photon Energy (eV)
Iron 1s XANES
b
Ferrihydrite
Goethite
Biogenic Oxide
Fluff layer
7048
7148
7248
7348
Photon Energy (eV)
Manganese 1s XANES
c
Δ-MnO2
Mn2O3
Mn3O4
Fluff layer
6476
6576
6676
6776
Photon Energy (eV)

Fig.3

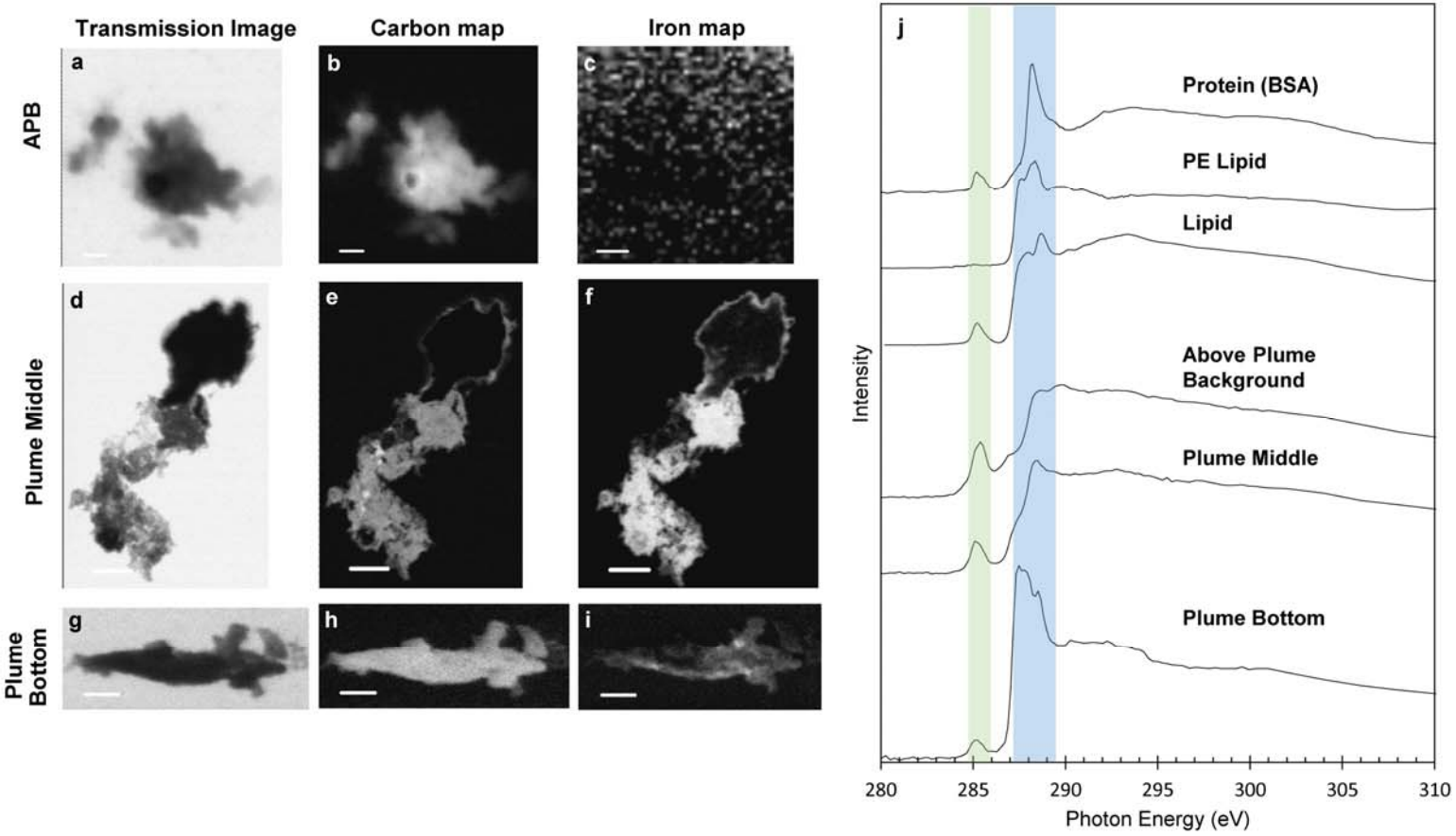
Transmission Image
Carbon map
Iron map
APB
Plume Middle
Plume Bottom
a
b
c
d
e
f
g
h
i
j
Protein (BSA)
PE Lipid
Lipid
Above Plume Background
Plume Middle
Plume Bottom
Intensity
280
285
290
295
300
305
310
Photon Energy (eV)

Fig.4

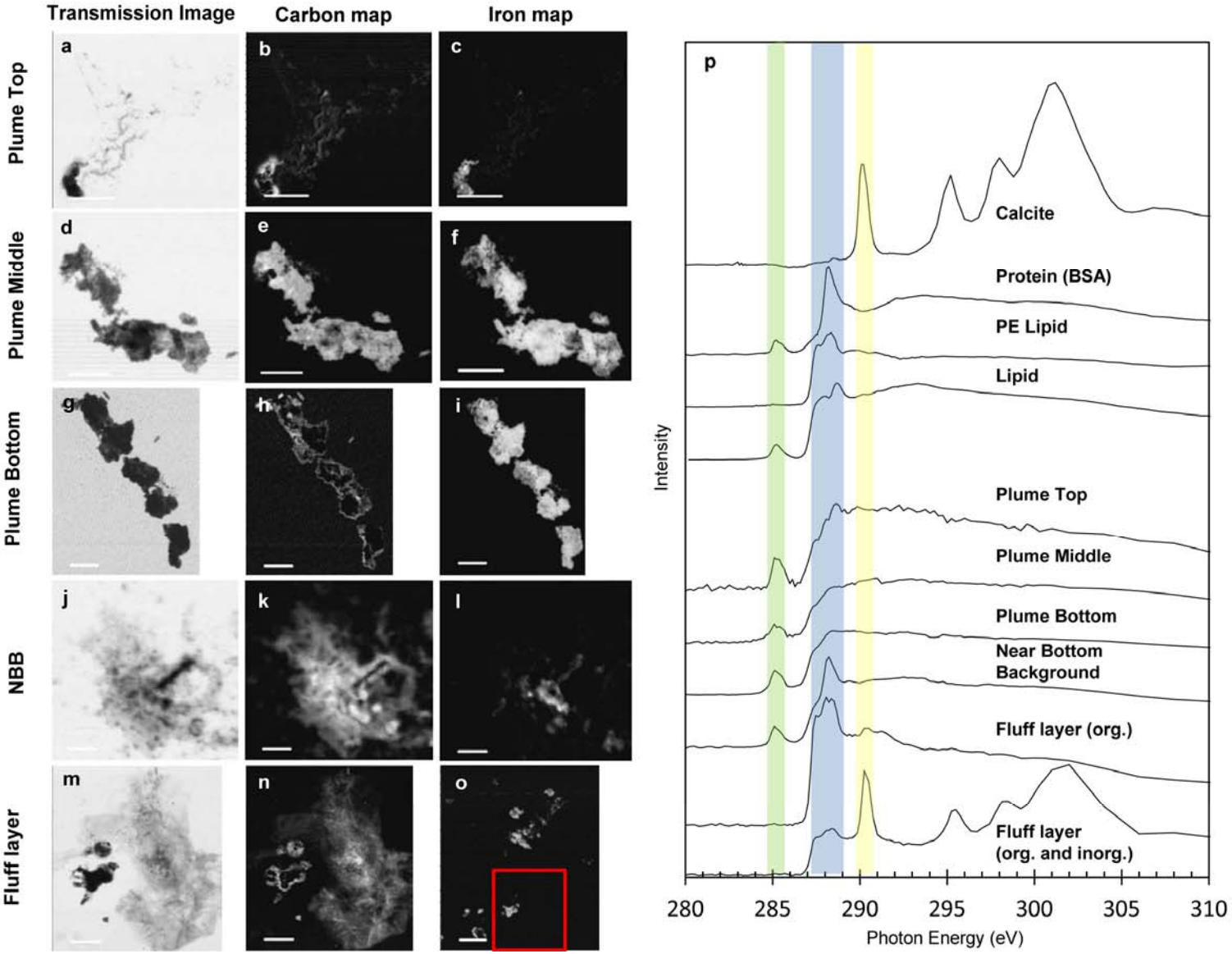
Transmission Image
Carbon map
Iron map
Plume Top
Plume Middle
Plume Bottom
NBB
Fluff layer
a
b
c
d
e
f
g
h
i
j
k
l
m
n
o
p
Calcite
Protein (BSA)
PE Lipid
Lipid
Plume Top
Plume Middle
Plume Bottom
Near Bottom
Background
Fluff layer (org.)
Fluff layer
(org. and inorg.)
Intensity
280
285
290
295
300
305
310
Photon Energy (eV)

Fig.5

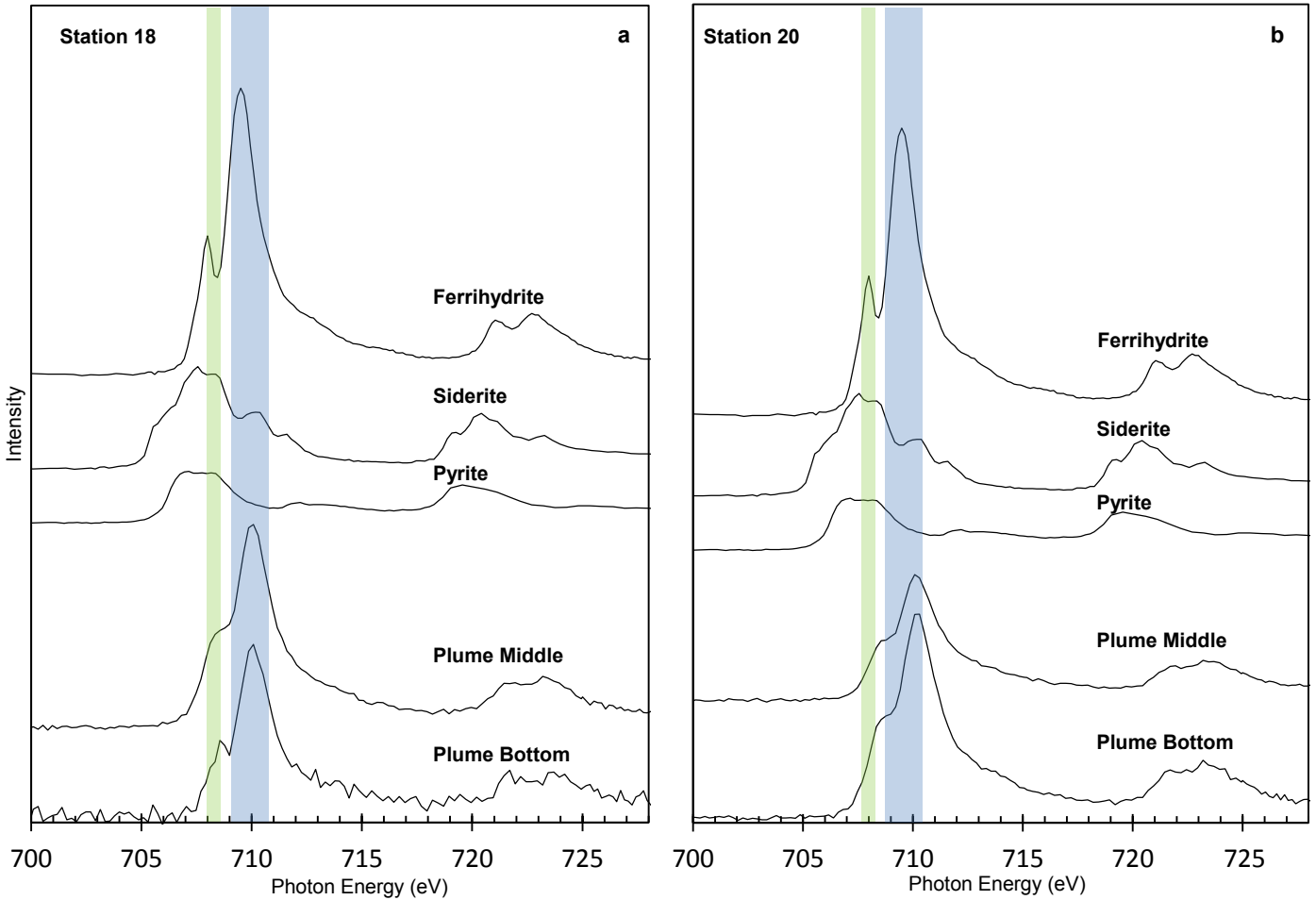
Station 18
a
Ferrihydrite
Siderite
Pyrite
Plume Middle
Plume Bottom
Intensity
700
705
710
715
720
725
Photon Energy (eV)
Station 20
b
Ferrihydrite
Siderite
Pyrite
Plume Middle
Plume Bottom
700
705
710
715
720
725
Photon Energy (eV)

Fig.6

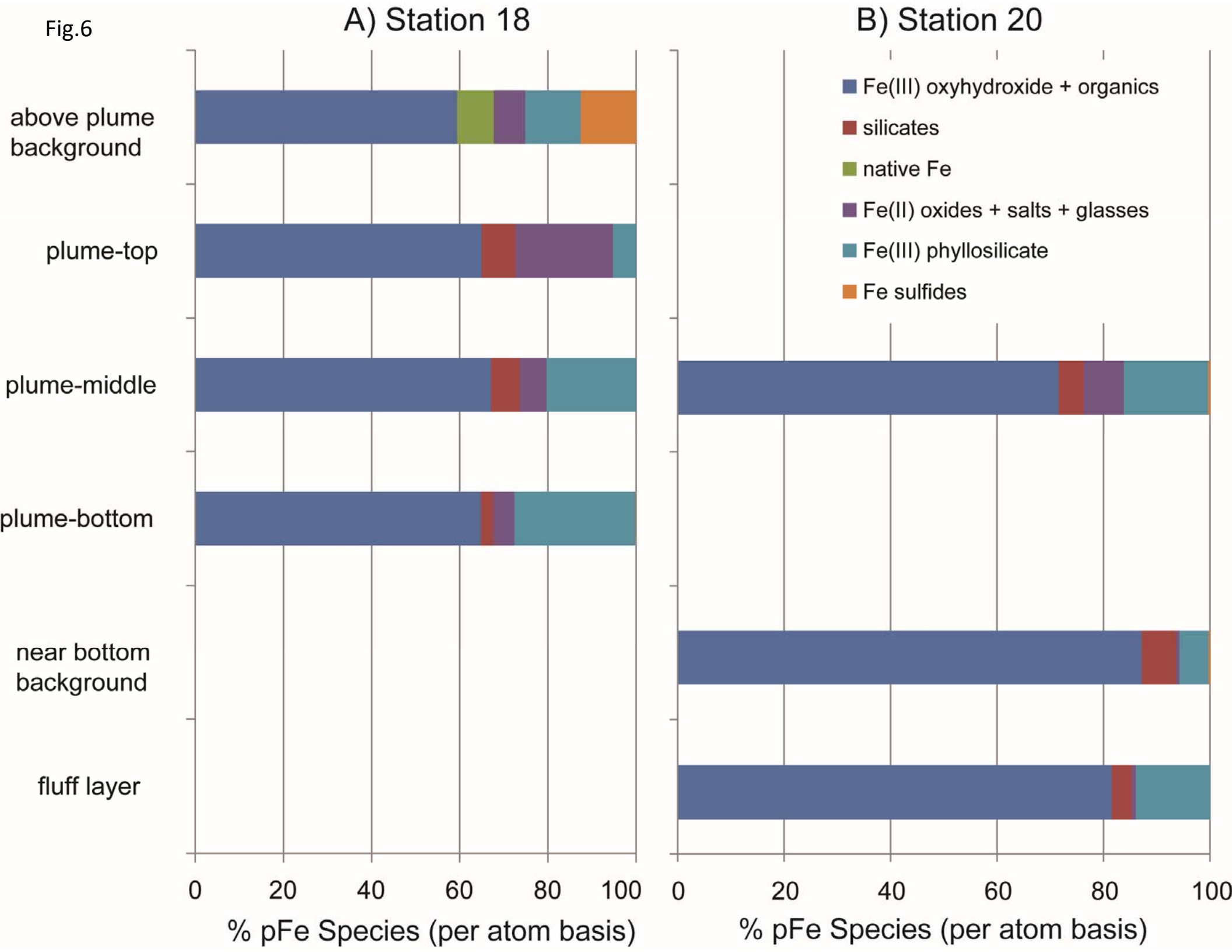
A) Station 18
B) Station 20
above plume background
plume-top
plume-middle
plume-bottom
near bottom background
fluff layer
Fe(III) oxyhydroxide + organics
silicates
native Fe
Fe(II) oxides + salts + glasses
Fe(III) phyllosilicate
Fe sulfides
0
20
40
60
80
100
% pFe Species (per atom basis)
% pFe Species (per atom basis)

Supplemental Table 1: Fe 1s XAS mineral classifications of post-fit fittings

standard nickname	standard full name	post-fit bins
gehlenite	gehlenite	silicate
moldavite	moldavite	Fe(II)
pyrite	pyrite	Fe sulfide
roedderite	roedderite	silicate
feso4	iron(II) sulfate	Fe(II)
basaltNKT	iron(II) glass	Fe(II)
clayFS	ferrosmectite	Fe(III)phyllosilicate
chromite	chromite	Fe(II)oxide
awaruite	awaruite	native Fe
maghemite	maghemite	Fe(III)oxide
fes	iron(II) monosulfide	Fe sulfide
lep	lepidocrocite	Fe(III)oxyhydroxide and organics
fhKIM	ferrihydrite-kim	Fe(III)oxyhydroxide and organics
fecl3	iron(III) chloride	Fe(III)oxyhydroxide and organics
andradite	andradite	silicate
richterite	richterite	silicate
perovskite	perovskite	Fe(II)oxide
bio	biogenic Fe(III) oxyhydroxide	Fe(III)oxyhydroxide and organics
alginate	iron(III) alginate	Fe(III)oxyhydroxide and organics
dextran	iron(III) dextran	Fe(III)oxyhydroxide and organics
pseudobrookite	pseudobrookite	Fe(III)oxide
goe	goethite	Fe(III)oxyhydroxide and organics
claySTX	montmorillonite	Fe(III)phyllosilicate
fh	ferrihydrite-toner	Fe(III)oxyhydroxide and organics

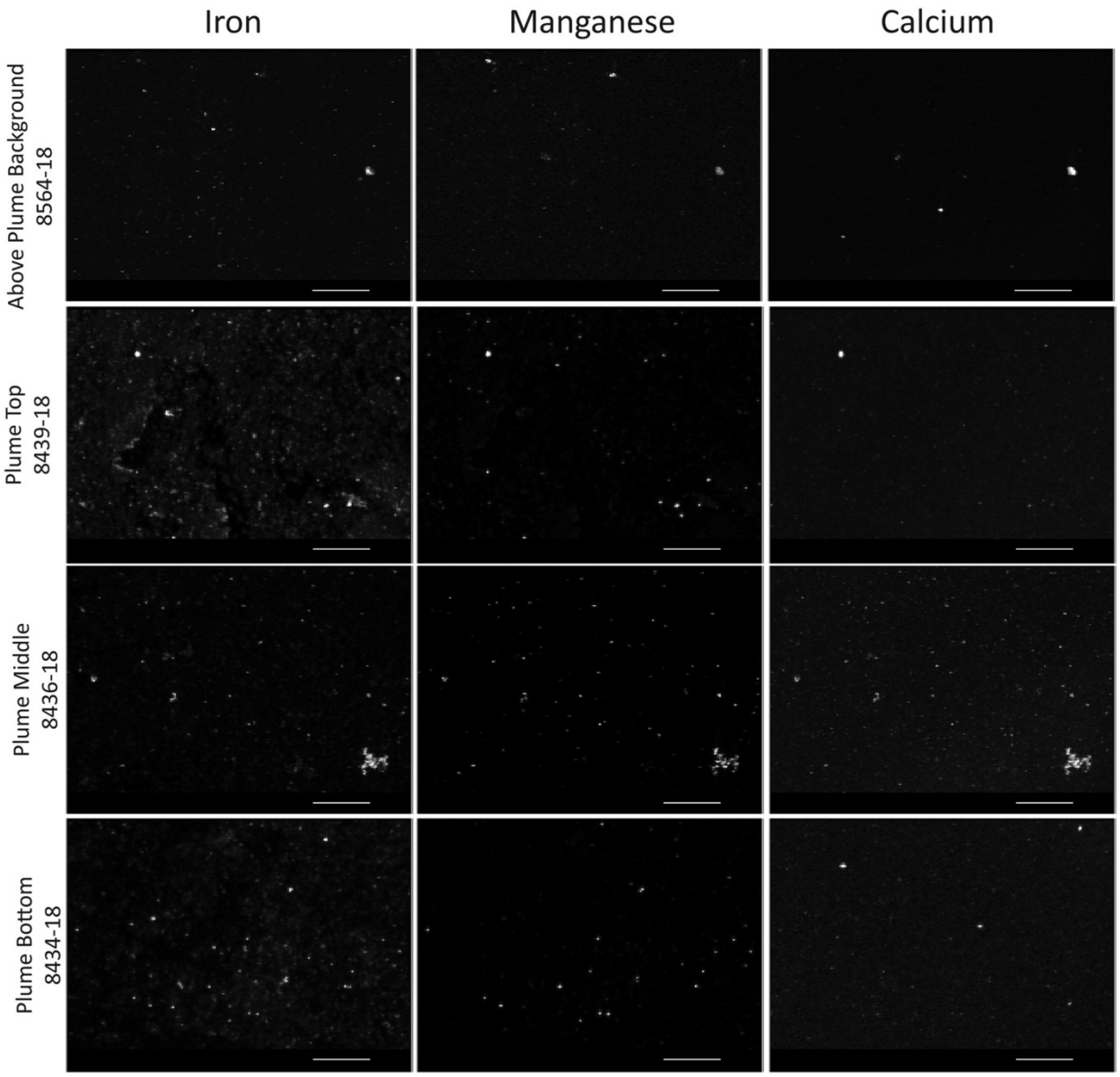

Fig. S1. X-ray fluorescence (XRF) maps of total iron, total manganese, and total calcium for the above plume background and top, middle, and bottom plume samples at Station 18. All scale bars 200 μm.

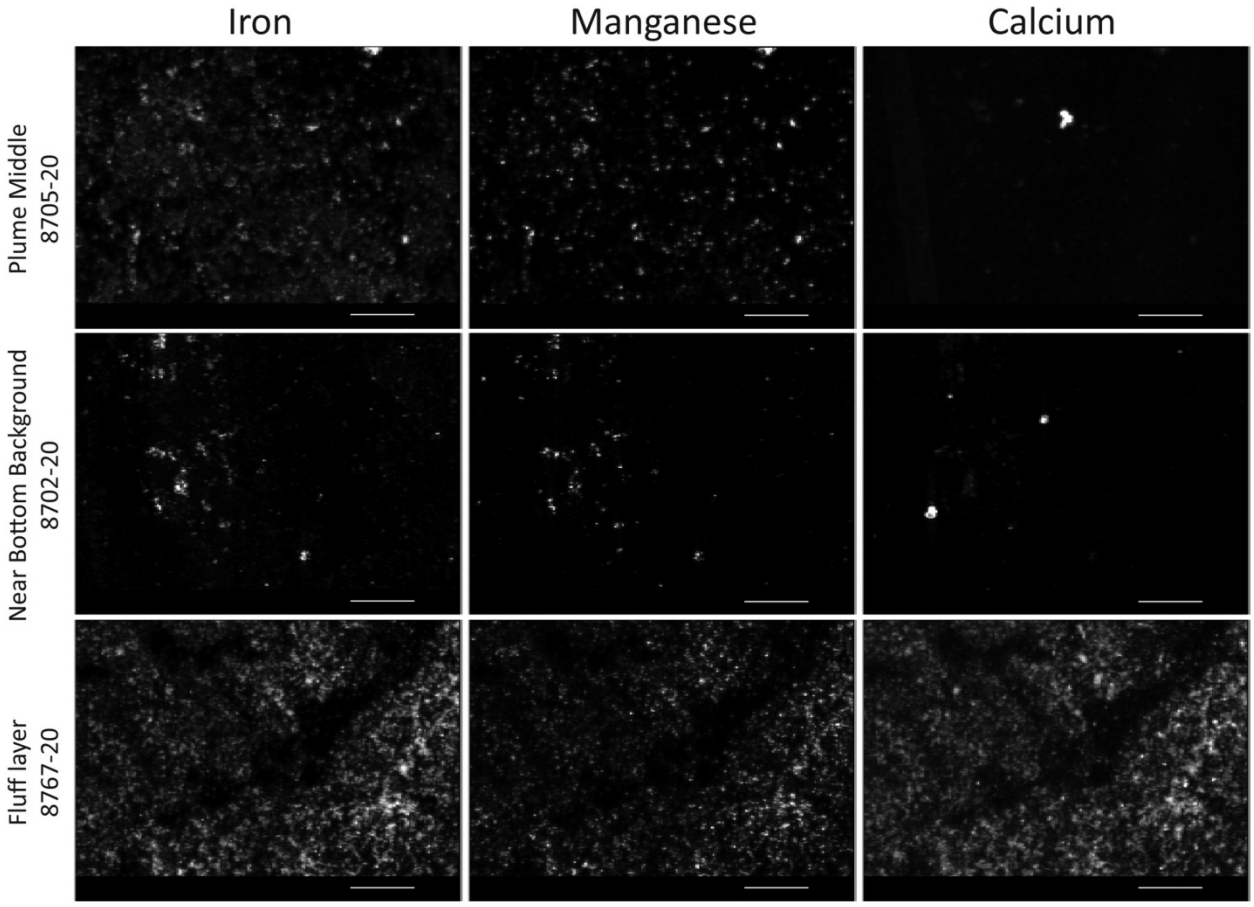

Fig. S2. X-ray fluorescence (XRF) maps of total iron, total manganese, and total calcium for the plume middle, near bottom background, and benthic fluff layer samples at Station 20. All scale bars 200 µm.

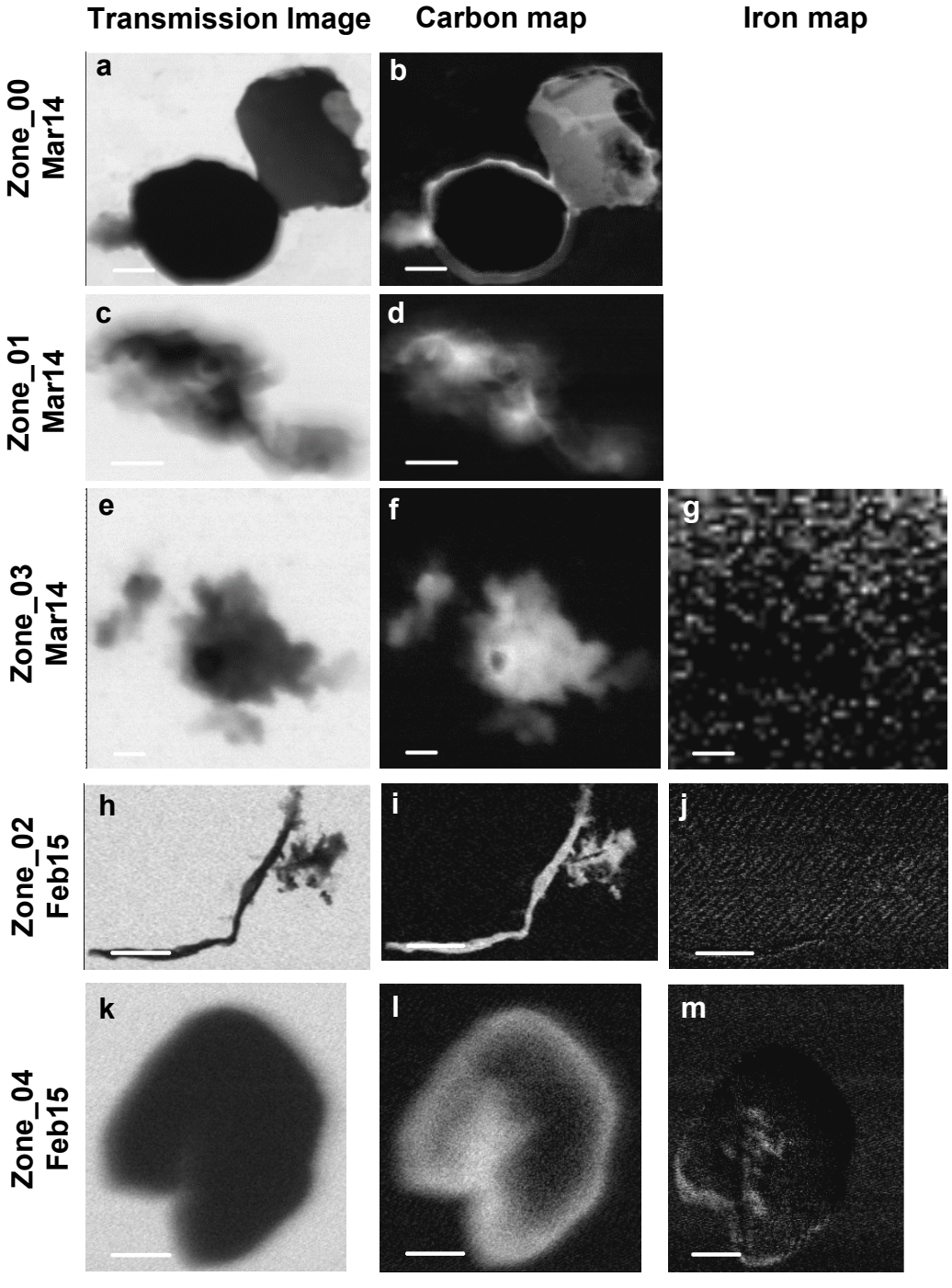
Transmission Image
Carbon map
Iron map
Zone_00 Mar14
Zone_01 Mar14
Zone_03 Mar14
Zone_02 Feb15
Zone_04 Feb15
a
b
c
d
e
f
g
h
i
j
k
l
m

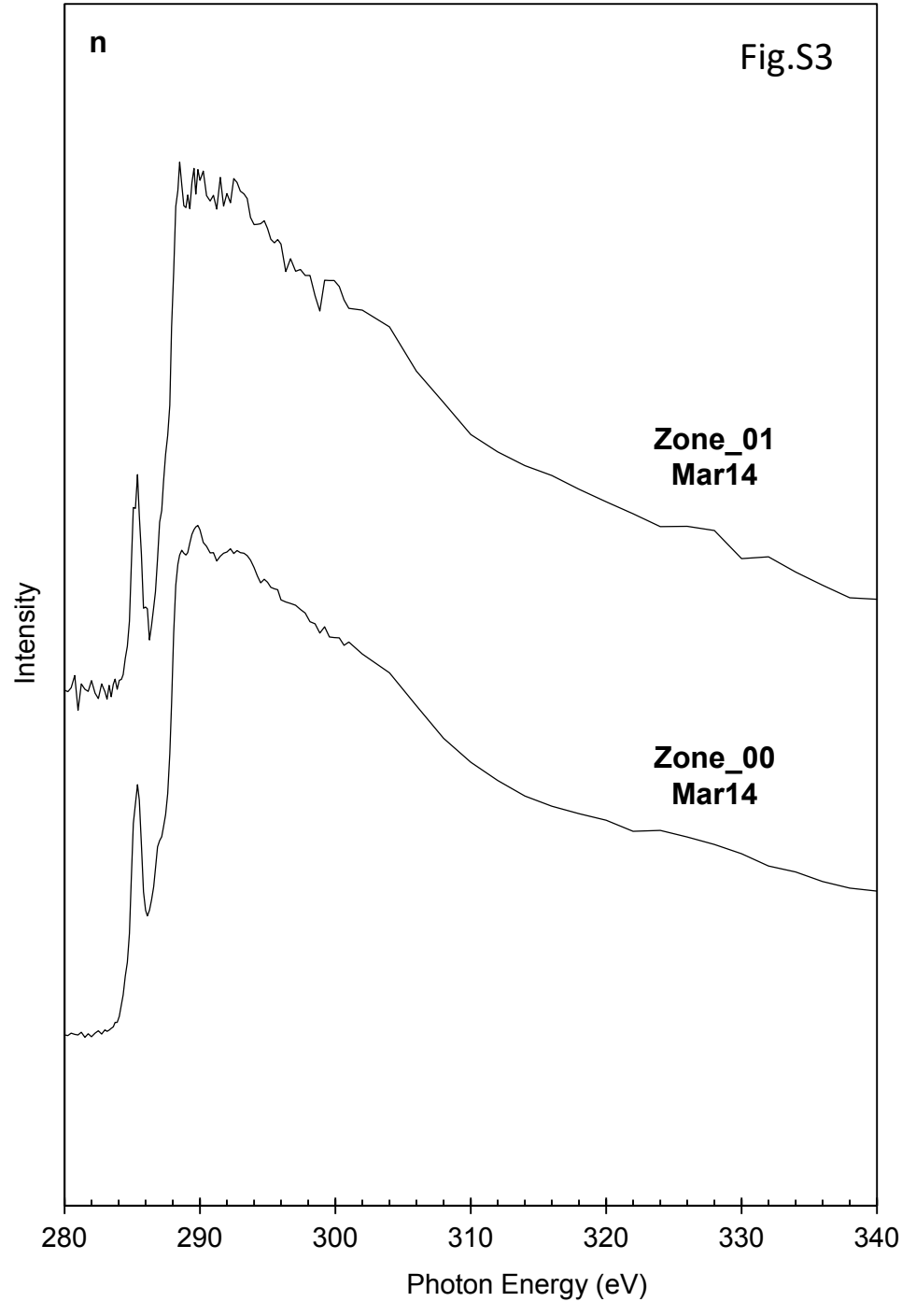
n
Fig.S3
Zone_01 Mar14
Zone_00 Mar14
Intensity
280
290
300
310
320
330
340
Photon Energy (eV)

Fig. S4

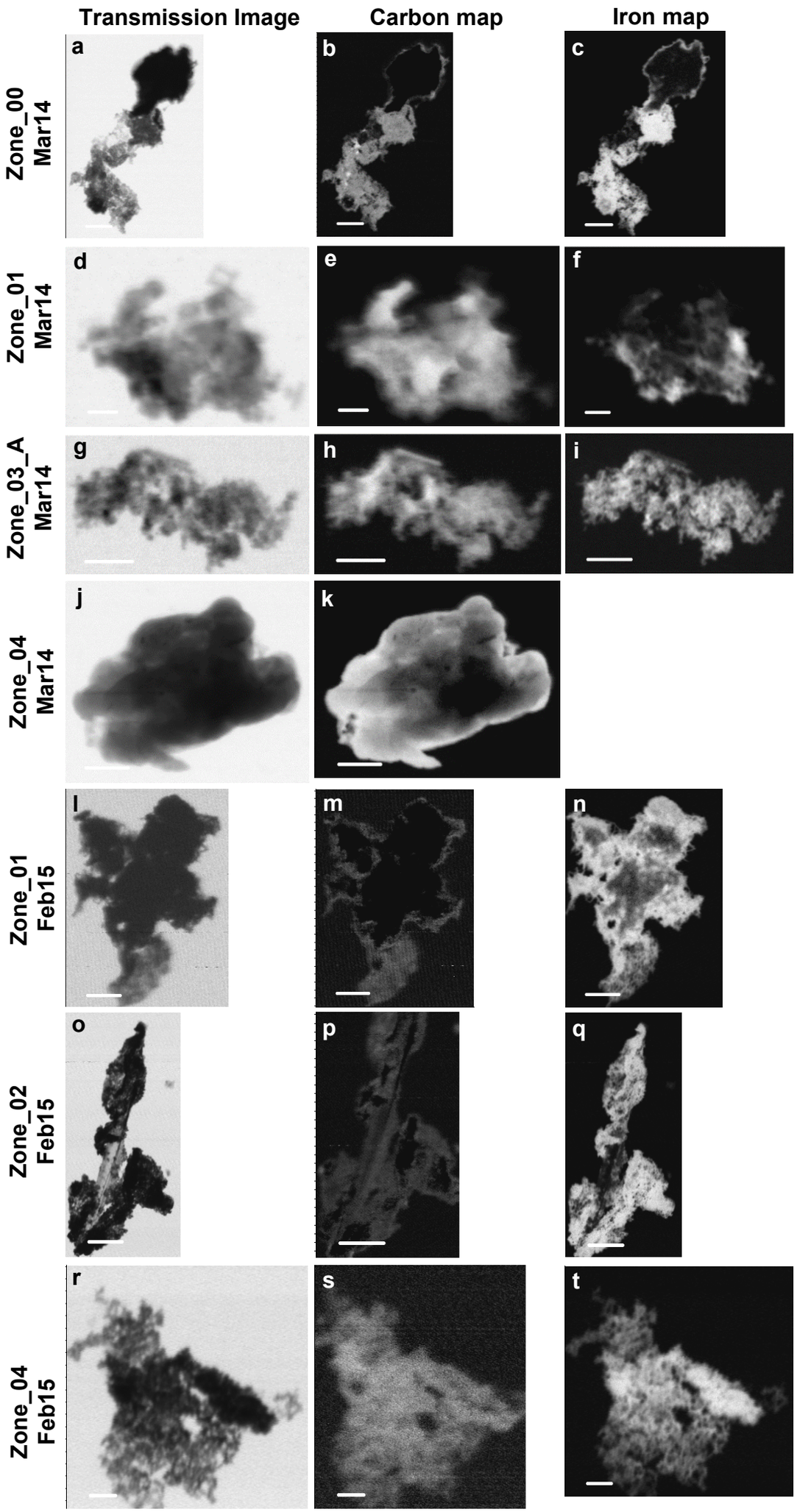
Transmission Image
Carbon map
Iron map
Zone_00 Mar14
Zone_01 Mar14
Zone_03_A Mar14
Zone_04 Mar14
Zone_01 Feb15
Zone_02 Feb15
Zone_04 Feb15
a
b
c
d
e
f
g
h
i
j
k
l
m
n
o
p
q
r
s
t

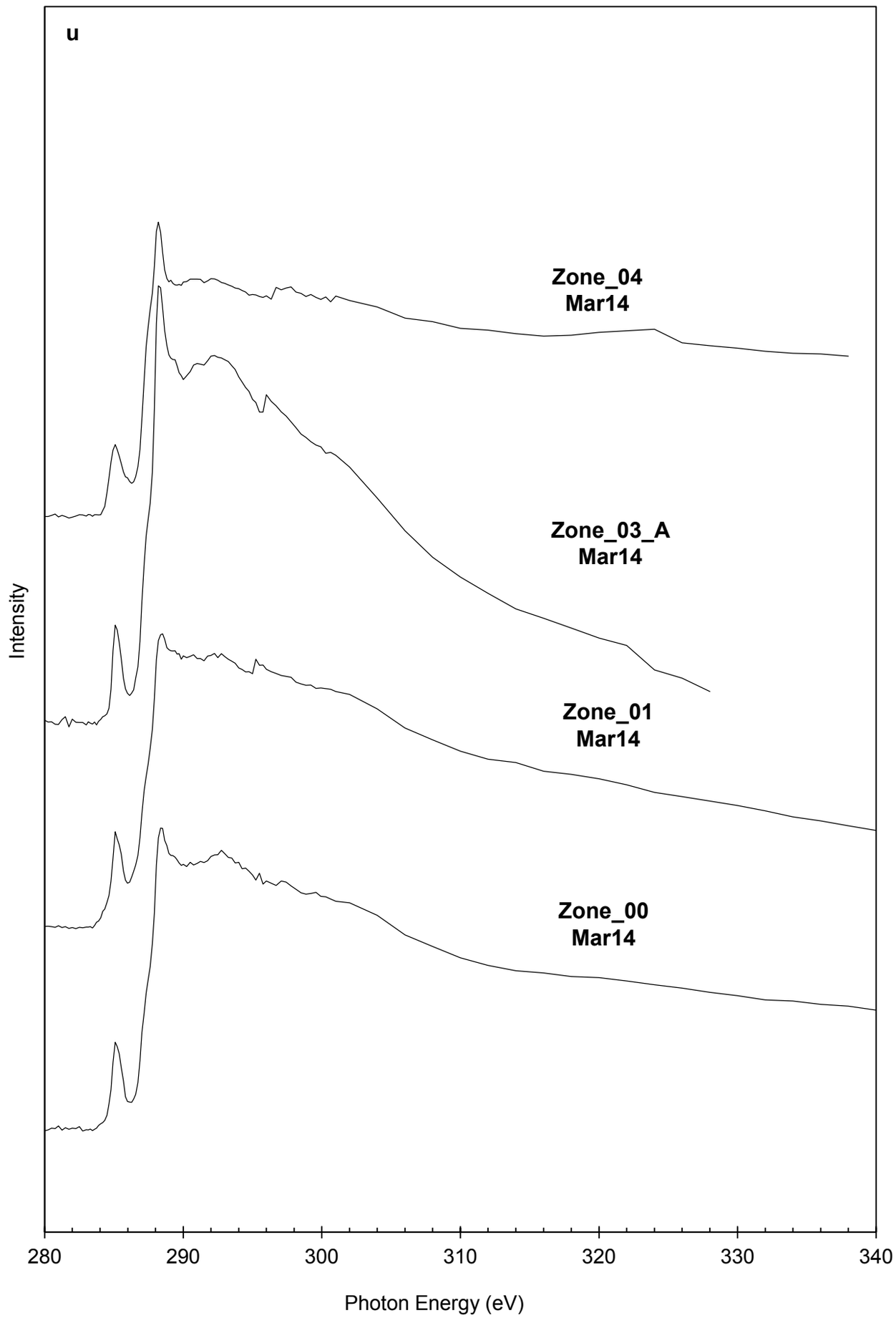
u
Zone_04 Mar14
Zone_03_A Mar14
Zone_01 Mar14
Zone_00 Mar14
Intensity
280
290
300
310
320
330
340
Photon Energy (eV)

Fig. S5

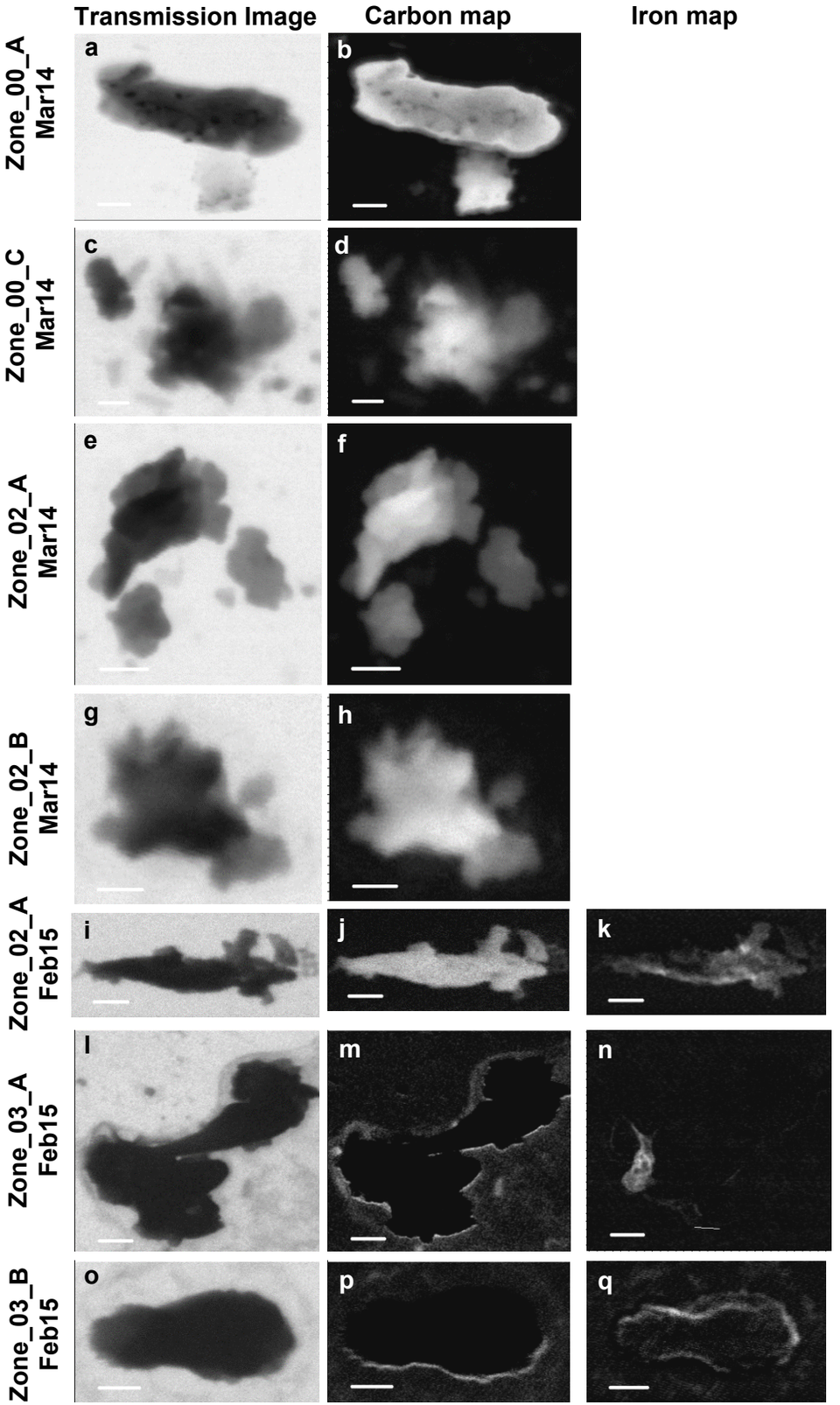
Transmission Image
Carbon map
Iron map
Zone_00_A Mar14
Zone_00_C Mar14
Zone_02_A Mar14
Zone_02_B Mar14
Zone_02_A Feb15
Zone_03_A Feb15
Zone_03_B Feb15
a
b
c
d
e
f
g
h
i
j
k
l
m
n
o
p
q

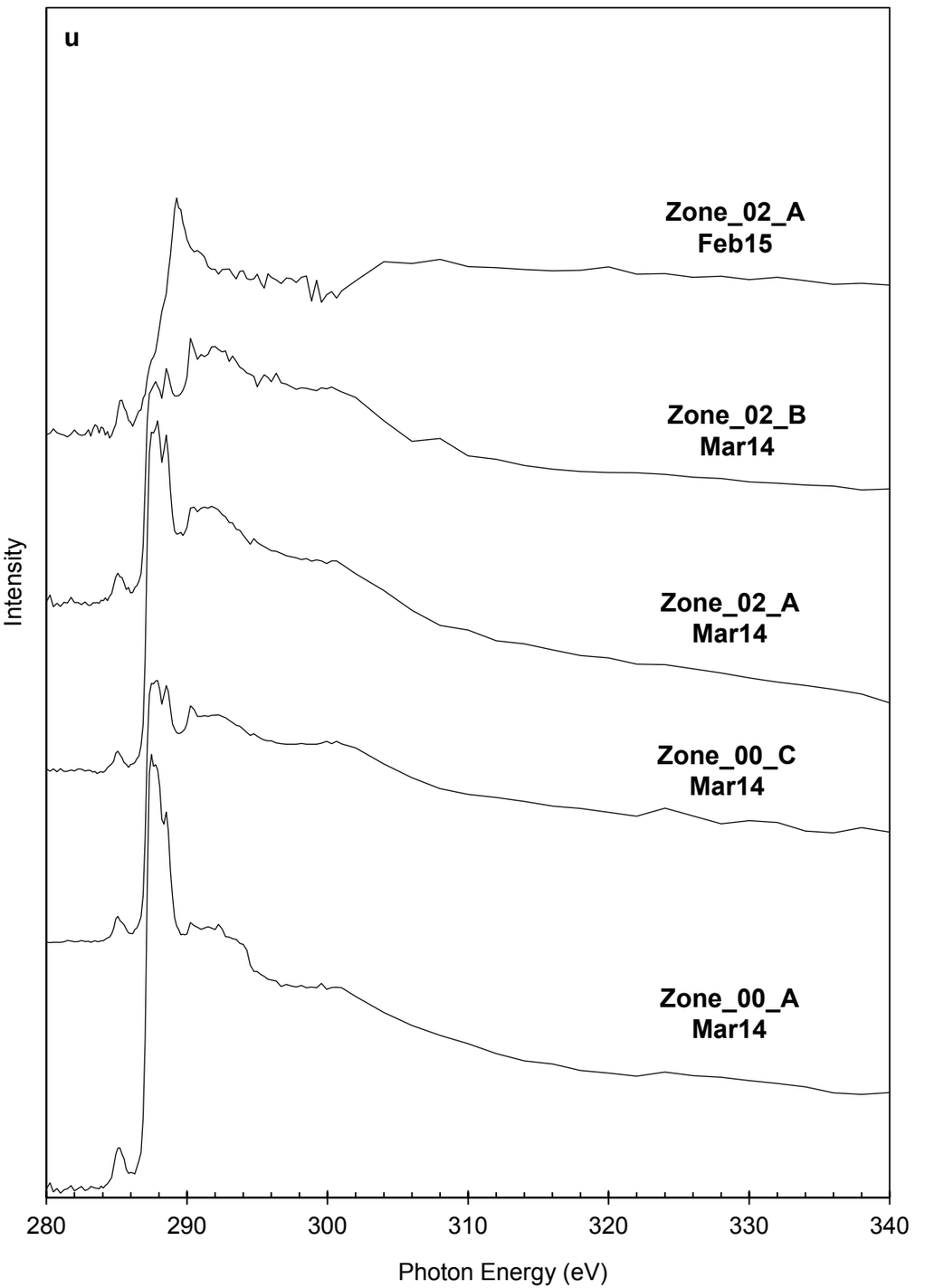
u
Zone_02_A Feb15
Zone_02_B Mar14
Zone_02_A Mar14
Zone_00_C Mar14
Zone_00_A Mar14
Intensity
280
290
300
310
320
330
340
Photon Energy (eV)

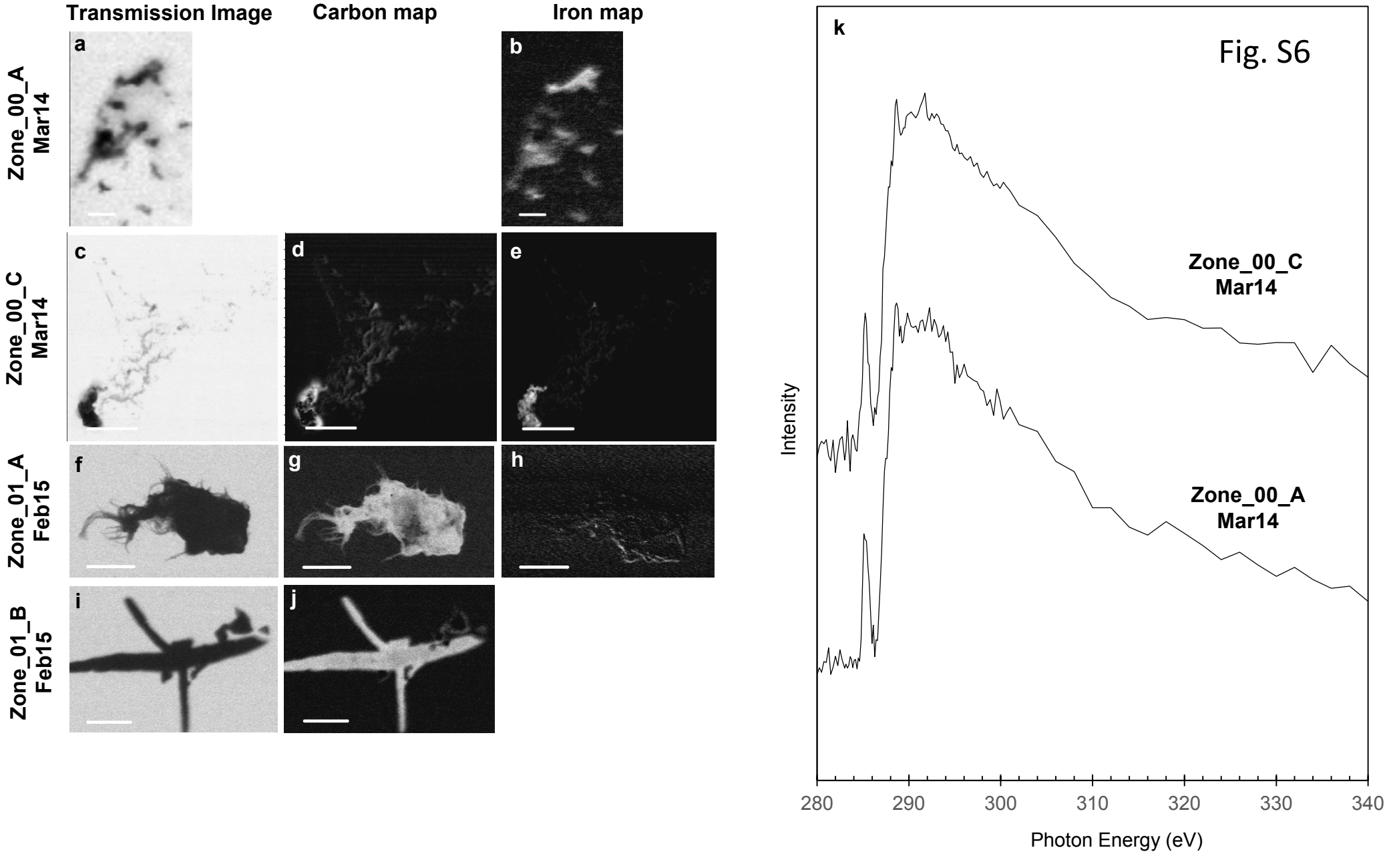
Transmission Image
Carbon map
Iron map
Zone_00_A Mar14
Zone_00_C Mar14
Zone_01_A Feb15
Zone_01_B Feb15
a
b
c
d
e
f
g
h
i
j
k
Fig. S6
Zone_00_C Mar14
Zone_00_A Mar14
Intensity
280
290
300
310
320
330
340
Photon Energy (eV)

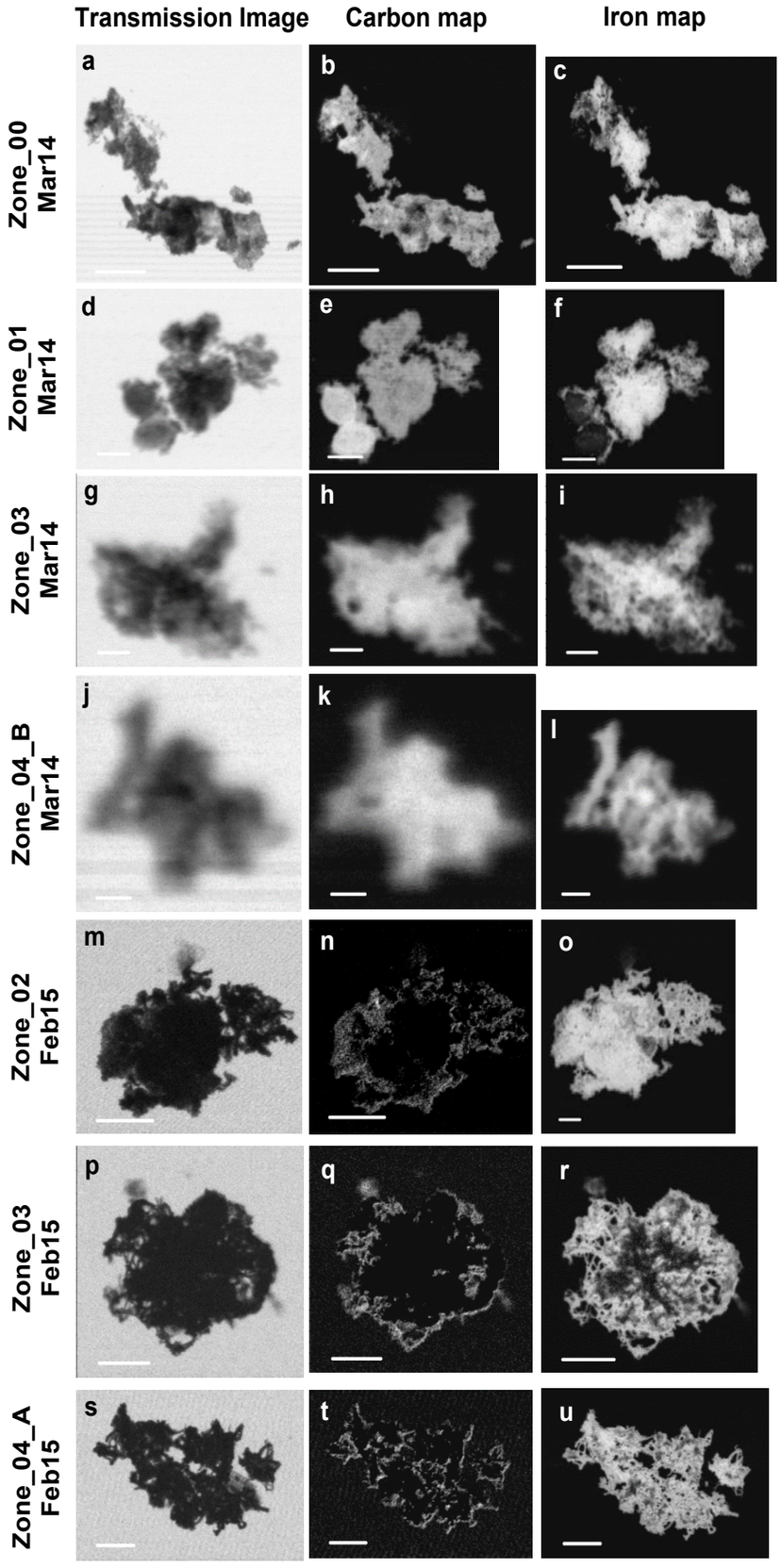
Transmission Image
Carbon map
Iron map
Zone_00 Mar14
Zone_01 Mar14
Zone_03 Mar14
Zone_04_B Mar14
Zone_02 Feb15
Zone_03 Feb15
Zone_04_A Feb15
a
b
c
d
e
f
g
h
i
j
k
l
m
n
o
p
q
r
s
t
u

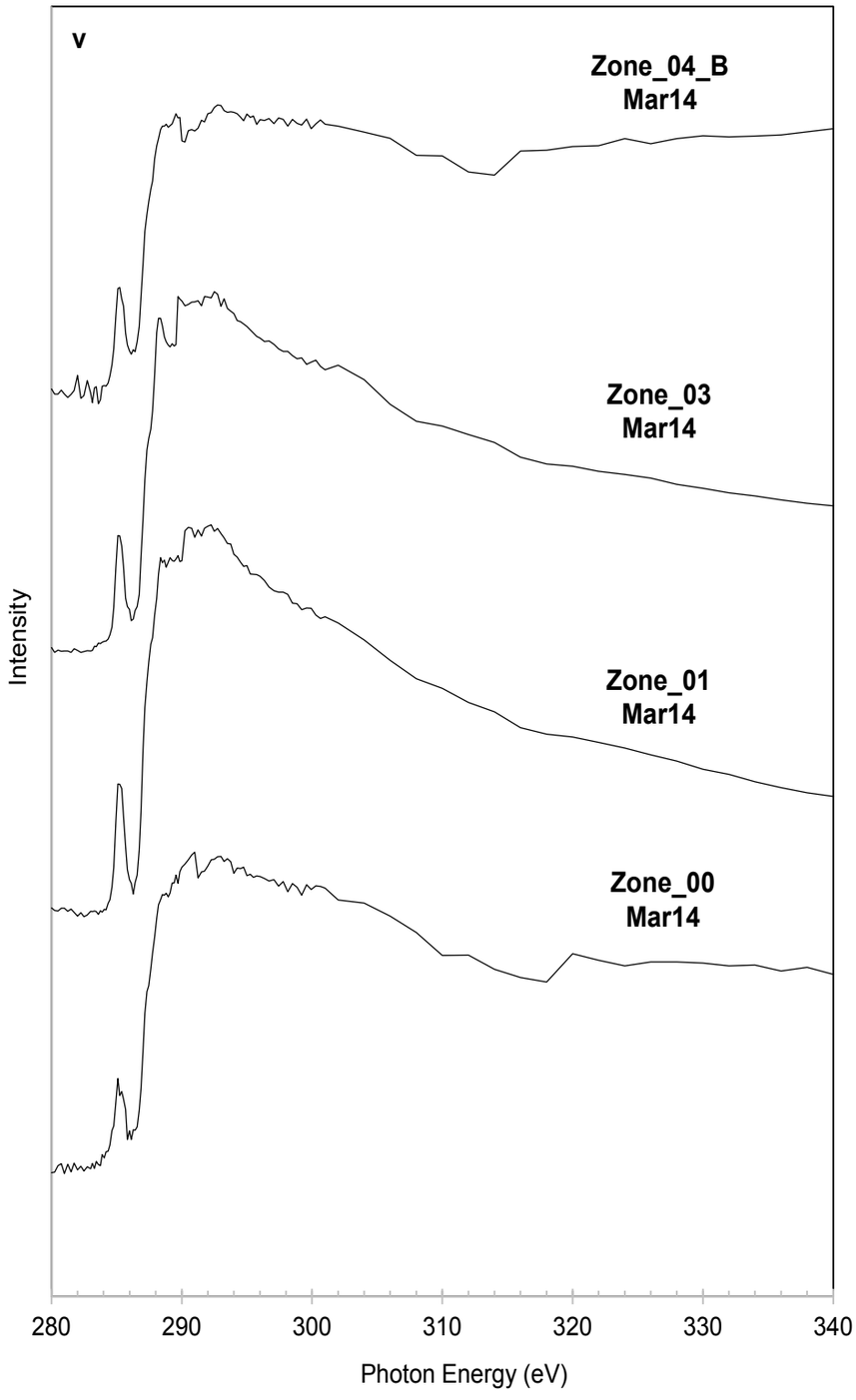
v
Zone_04_B Mar14
Zone_03 Mar14
Zone_01 Mar14
Zone_00 Mar14
Intensity
280
290
300
310
320
330
340
Photon Energy (eV)

Fig. S7

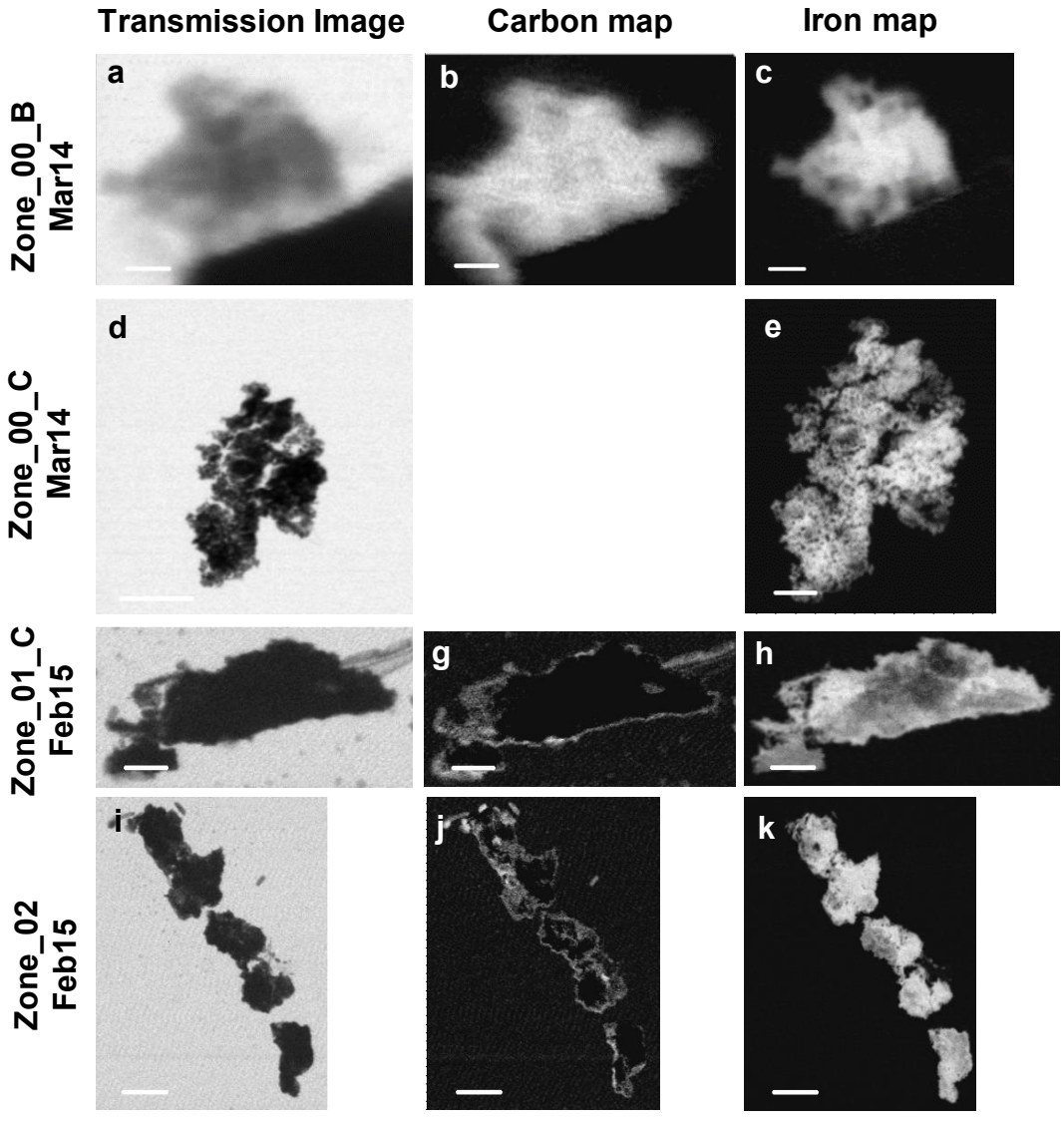
Transmission Image
Carbon map
Iron map
Zone_00_B Mar14
Zone_00_C Mar14
Zone_01_C Feb15
Zone_02 Feb15
a
b
c
d
e
g
h
i
j
k

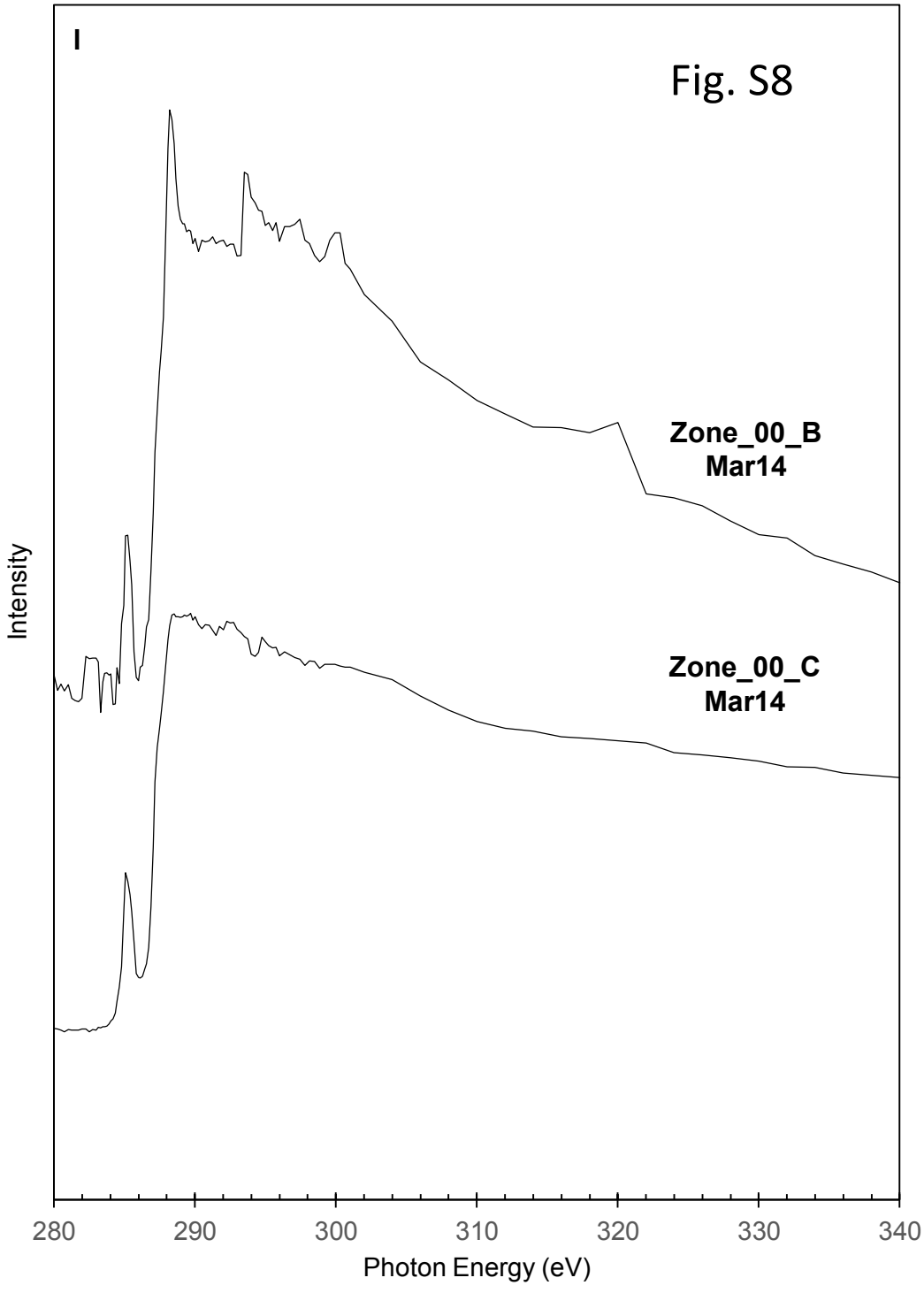
l
Fig. S8
Intensity
Zone_00_B Mar14
Zone_00_C Mar14
280
290
300
310
320
330
340
Photon Energy (eV)

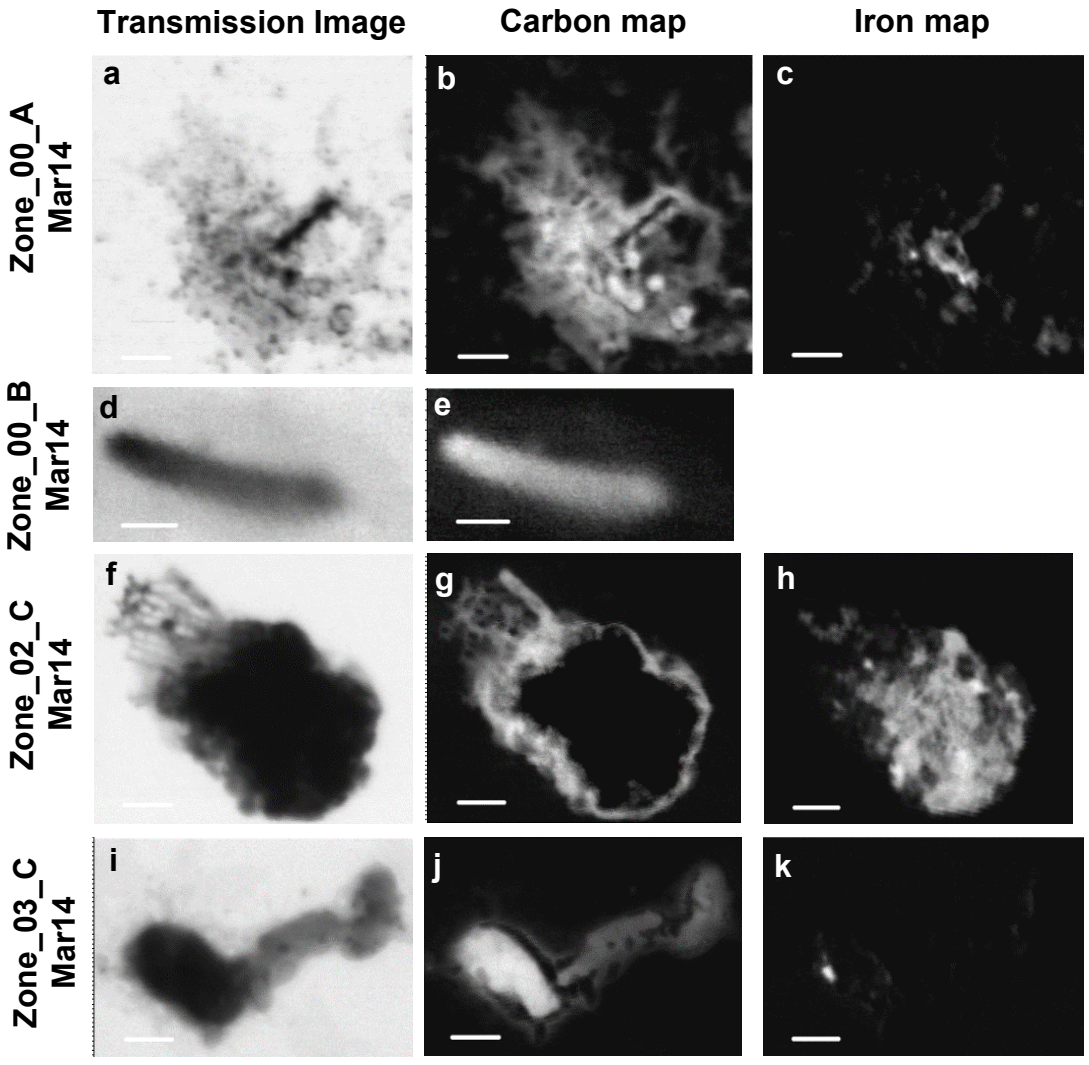
Transmission Image
Carbon map
Iron map
Zone_00_A Mar14
Zone_00_B Mar14
Zone_02_C Mar14
Zone_03_C Mar14
a
b
c
d
e
f
g
h
i
j
k

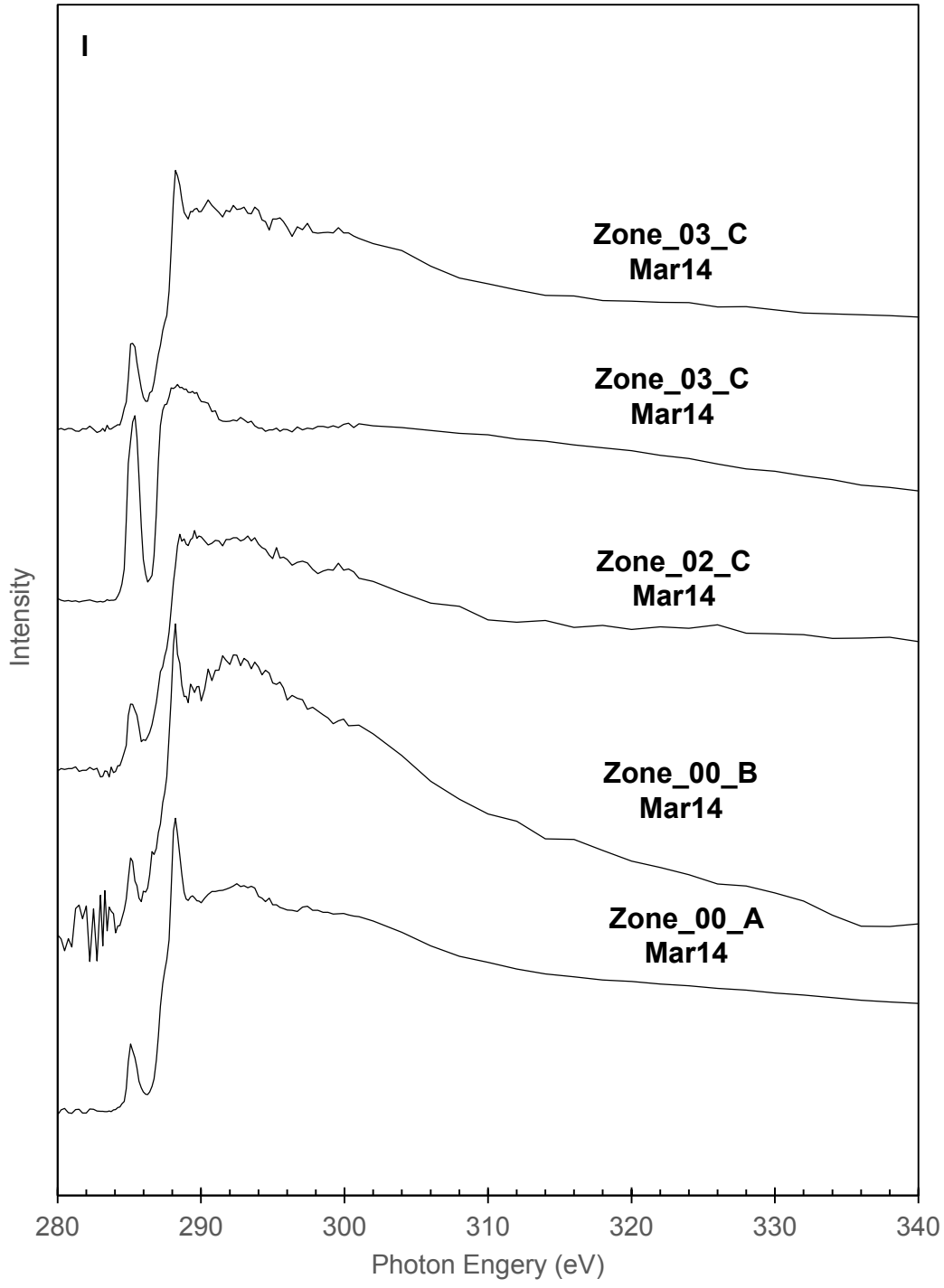
l
Zone_03_C Mar14
Zone_03_C Mar14
Zone_02_C Mar14
Zone_00_B Mar14
Zone_00_A Mar14
Intensity
280
290
300
310
320
330
340
Photon Engery (eV)

Fig. S9

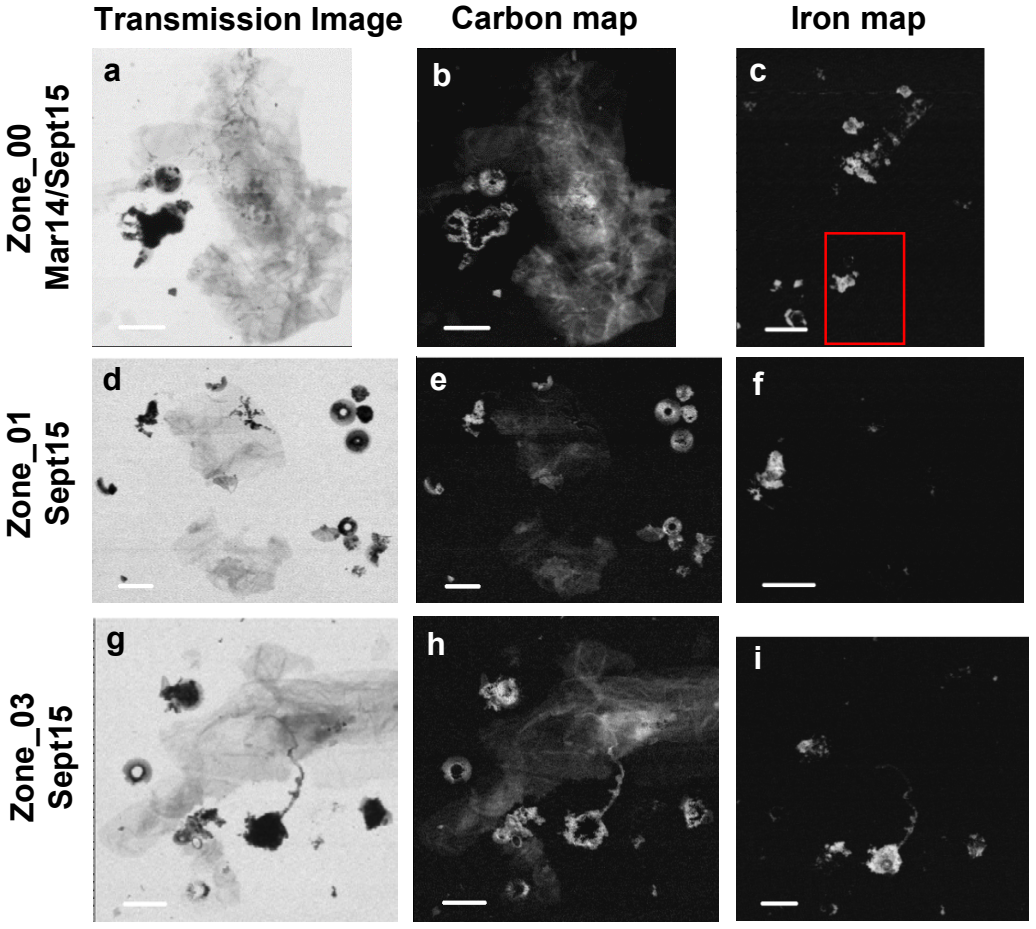
Transmission Image
Carbon map
Iron map
Zone_00 Mar14/Sept15
Zone_01 Sept15
Zone_03 Sept15
a
b
c
d
e
f
g
h
i

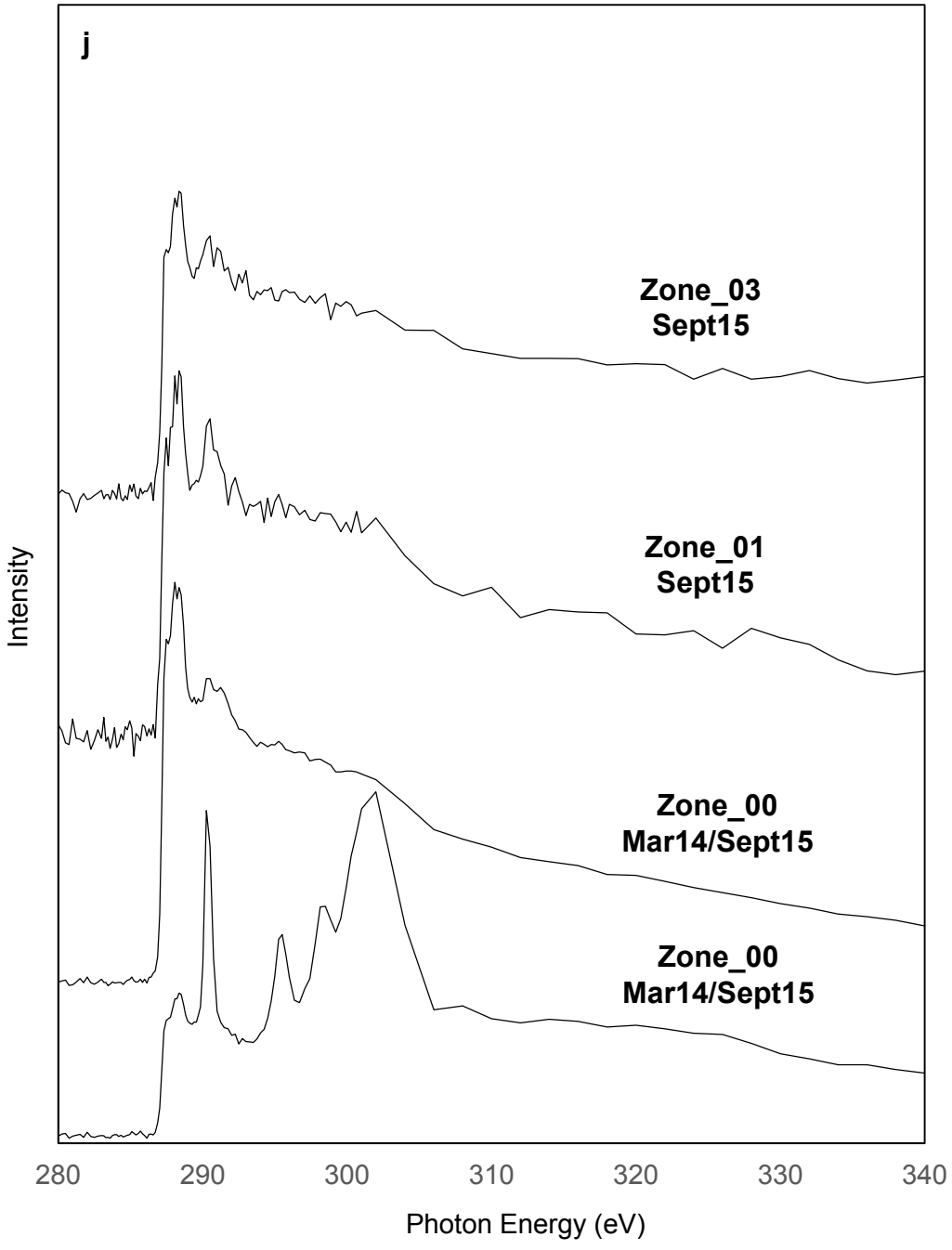
j
Intensity
Zone_03 Sept15
Zone_01 Sept15
Zone_00 Mar14/Sept15
Zone_00 Mar14/Sept15
280
290
300
310
320
330
340
Photon Energy (eV)

Fig. S10

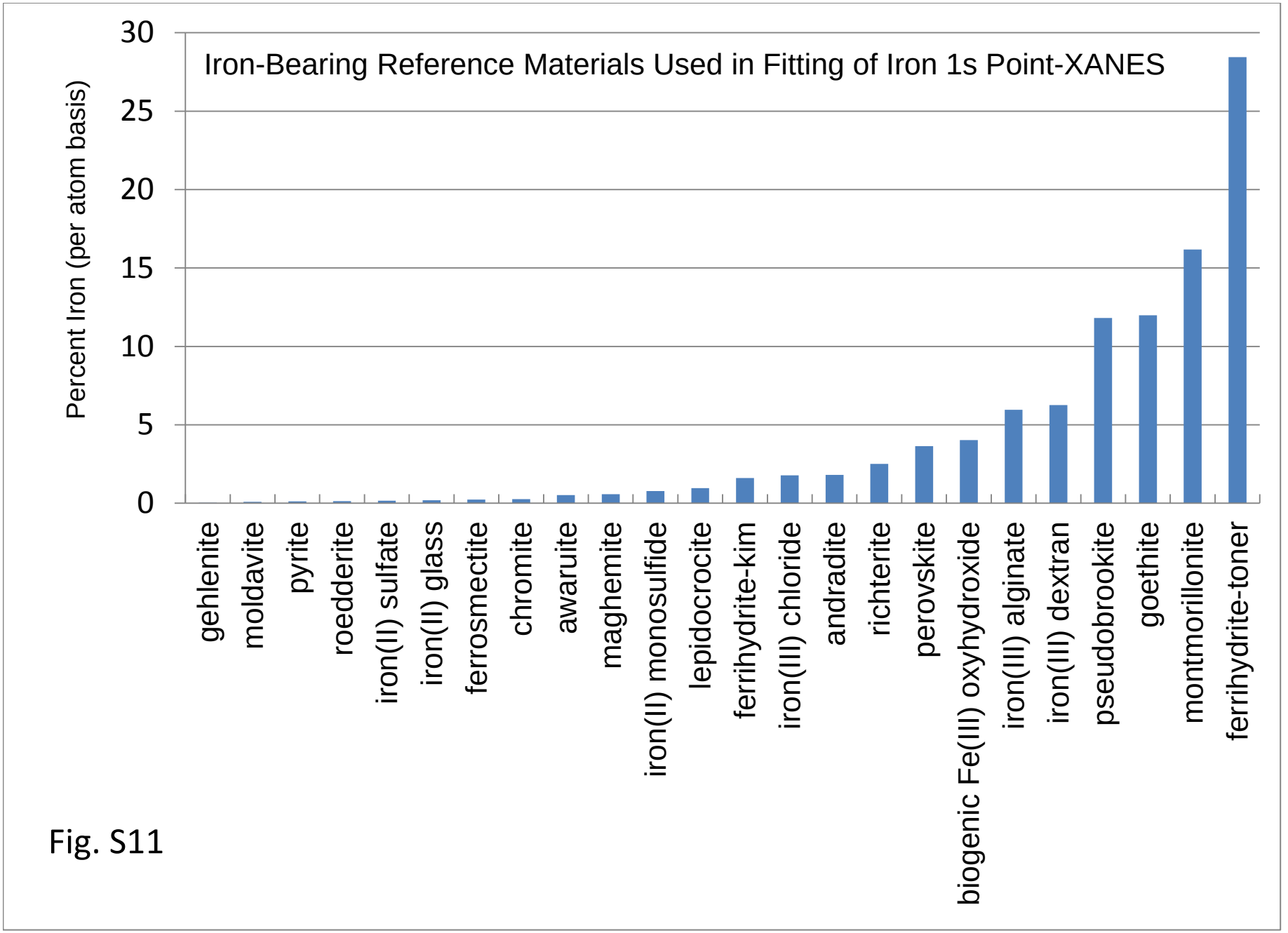
Iron-Bearing Reference Materials Used in Fitting of Iron 1s Point-XANES
Percent Iron (per atom basis)
30
25
20
15
10
5
0
gehlenite
moldavite
pyrite
roedderite
iron(II) sulfate
iron(II) glass
ferrosmectite
chromite
awaruite
maghemite
iron(II) monosulfide
lepidocrocite
ferrihydrite-kim
iron(III) chloride
andradite
richterite
perovskite
biogenic Fe(III) oxyhydroxide
iron(III) alginate
iron(III) dextran
pseudobrookite
goethite
montmorillonite
ferrihydrite-toner

Fig. S11

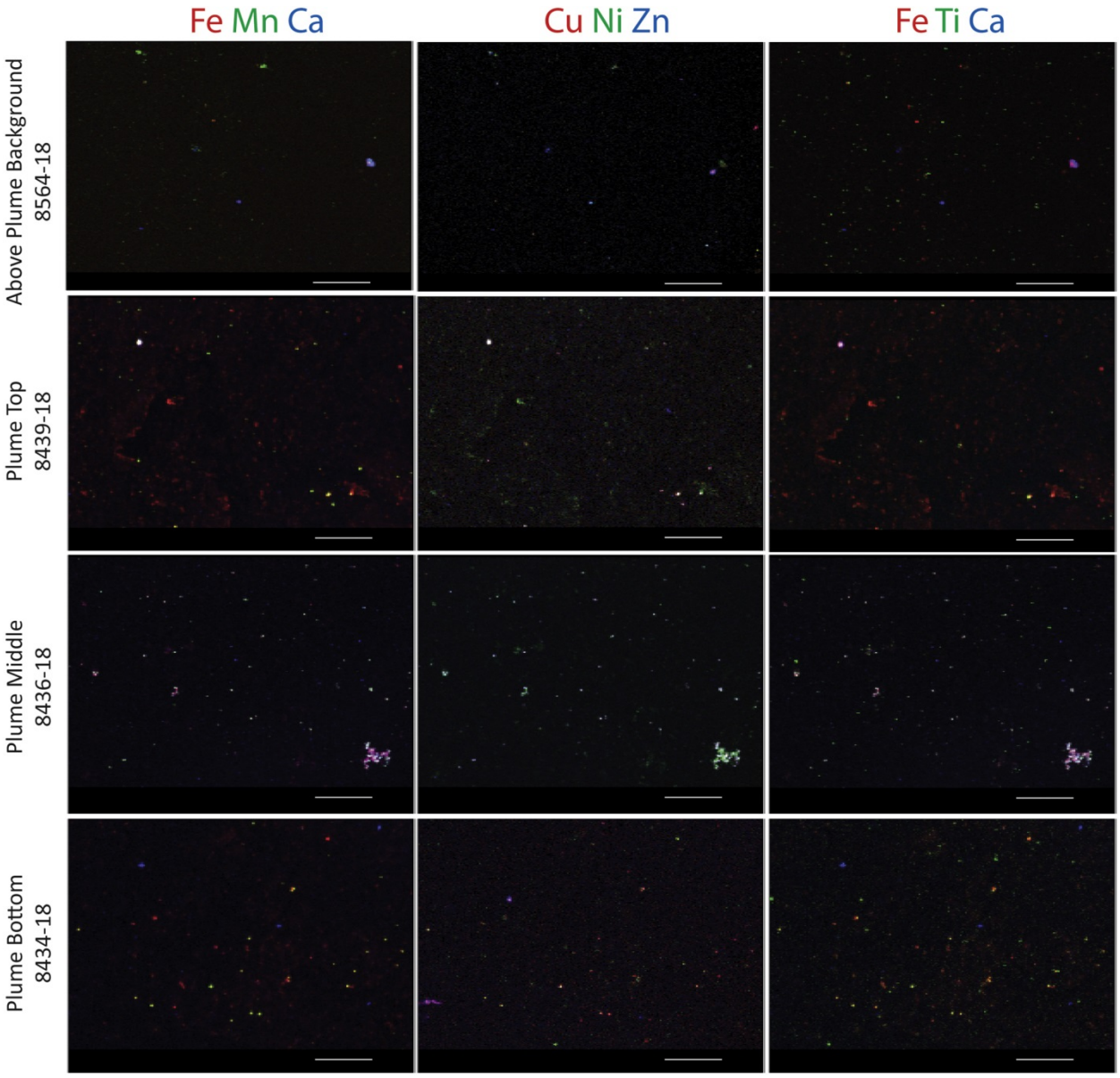

Fig. S12. X-ray fluorescence (XRF) tricolor maps for above plume background and top, middle, and bottom plume samples at Station 18. Column left (FeMnCa), center (CuNiZn), and right (FeTiCa) are shown in red, green, blue. All scale bars 200 µm.

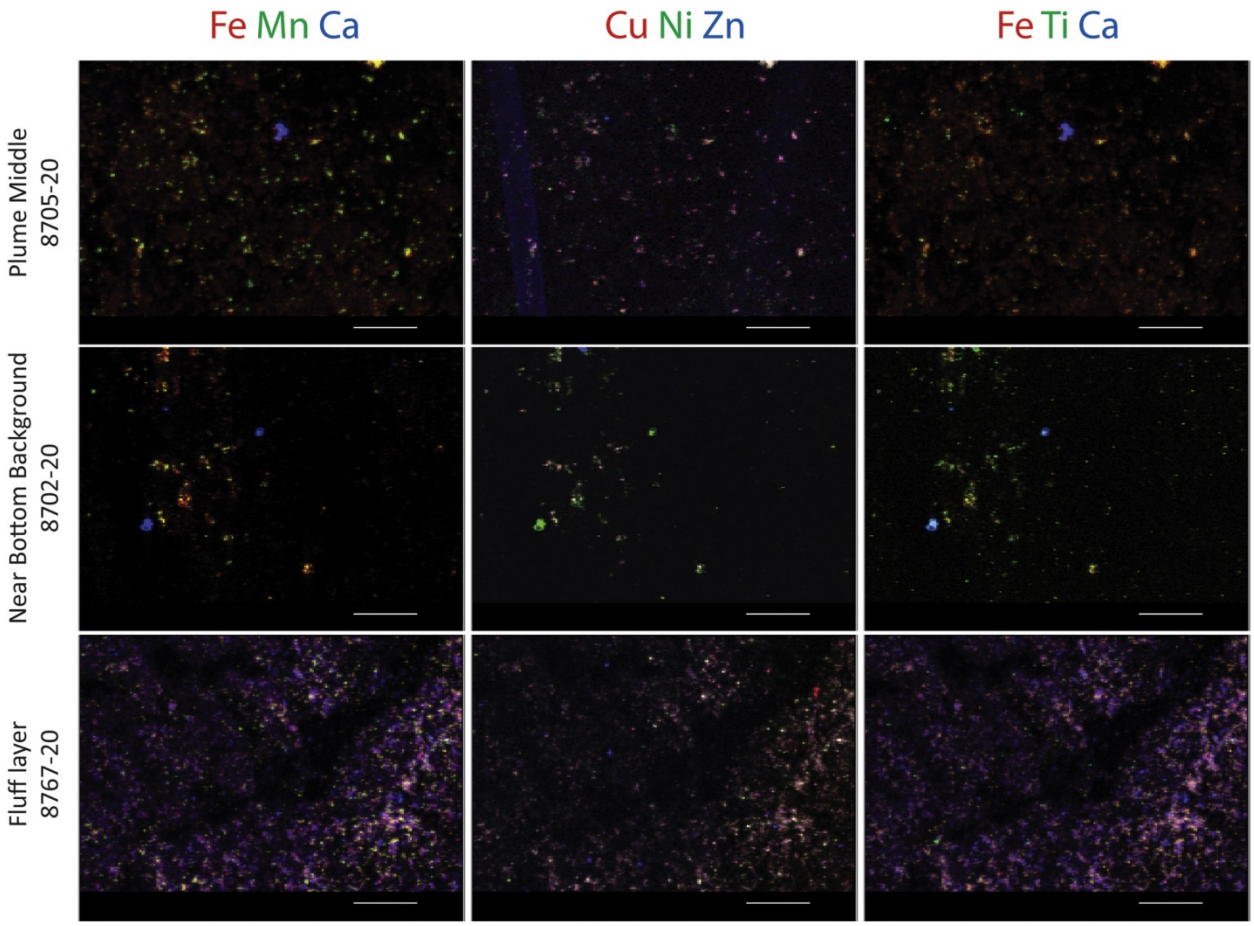

Fig. S13. X-ray fluorescence (XRF) tricolor maps for the plume middle, near bottom background, and benthic fluff layer samples at Station 20. Column left (FeMnCa), center (CuNiZn), and right (FeTiCa) are shown in red, green, blue. All scale bars 200 µm.